energies

Article

Assessment of Voltage Violation Risk in Distribution Networks Under Extreme High-Temperature Conditions with Multiphysics Field Coupling

Qinhua Chen [1,2,*], Jun He [1,2], Hongwei Deng [1,2], Penghui Yan [1,2], Xiaoyu Nie [1,2], Yifan Lv [1,2] and Shuyi Wang [1,2]

[1] School of Electrical and Electronic Engineering, Hubei University of Technology, Wuhan 430068, China; hejun@hbut.edu.cn (J.H.); 102410331@hbut.edu.cn (H.D.); 18253015836@163.com (P.Y.); 17835604748@163.com (X.N.); 18971204732@163.com (Y.L.); 19974075273@163.com (S.W.)
[2] Hubei Key Laboratory for High-Efficiency Utilization of Solar Energy and Operation Control of Energy Storage System, Hubei University of Technology, Wuhan 430068, China
* Correspondence: 102410316@hbut.edu.cn; Tel.: +86-173-6285-2278

Abstract

To address the low-voltage violations that may occur in distribution networks with high penetration of distributed photovoltaic (PV) during sunset and evening peak periods under extreme high-temperature conditions, this paper establishes a source–grid–load electro-thermal coupling model that accounts for load thermal accumulation, transient conductor thermal inertia, temperature-dependent line impedance, and PV thermal derating. Based on a soft safety lower bound and a risk-preference utility function, the probability of voltage violation, violation depth, and expected violation duration are introduced to construct node-level and system-level comprehensive risk factors. The cumulant method combined with the Cornish–Fisher expansion is used to reconstruct the probability distribution of nodal voltages, enabling analytical risk calculation. Simulation results on the IEEE 33-bus system at 45 °C show that the proposed method can quantitatively reflect the temporal variations of nodal voltage distributions, physical violation depth, dimensionless severity utility, and expected violation duration, and identify weak nodes in the later part of the evening peak, providing a reference for risk early warning in distribution networks under extreme heat.

Keywords: extreme high temperature; distribution network; voltage violation risk; multiphysics coupling; Cornish–Fisher expansion

Check for updates

Academic Editor: Pavlos S. Georgilakis

Received: 25 May 2026
Revised: 18 June 2026
Accepted: 18 June 2026
Published: 24 June 2026

Copyright: © 2026 by the authors. Licensee MDPI, Basel, Switzerland. This article is an open access article distributed under the terms and conditions of the Creative Commons Attribution (CC BY) license.

1. Introduction

The frequent occurrence of extreme high-temperature events has posed a significant threat to the secure operation of power systems [1]. In 2022, the extreme heat and drought in Sichuan led to a surge in air-conditioning load and a sharp drop in hydropower output, exposing the vulnerability of the power grid under extreme weather [2]. With the continuous increase in distributed PV penetration, the low-voltage risk in distribution networks under extreme heat is becoming more prominent: high temperature pushes up the demand of temperature-sensitive loads, while the efficiency of PV modules declines due to temperature rise, weakening local support after sunset and severely compressing the voltage safety margin at feeder ends [3]. Accurately quantifying the time-varying voltage violation risk in distribution networks under extreme heat is of great significance for ensuring the safe operation of new-type power systems.

Regarding extreme scenarios, existing studies have conducted valuable explorations from the perspectives of resilience assessment and supply–demand balance. Reference [4] constructed a resilience assessment framework for new power systems under extreme high temperatures, Ref. [5] proposed a resilience quantification method for distribution networks covering the whole process of prevention, resistance, and recovery, Ref. [6] evaluated the system supply–demand balance capability under extreme heat scenarios, and Ref. [7] studied the resilience enhancement strategy of cable-type distribution networks. The above works focus on system-level indicators and pay insufficient attention to node-level voltage violation risk assessment.

In the area of voltage violation risk assessment, methods such as the cumulant method combined with the Cornish–Fisher expansion, sparse polynomial chaos expansion with Lasso regression, etc., have been used to analytically reconstruct probability distributions. Techniques such as polynomial chaos Kriging models, quasi-sequential Monte Carlo simulation, and Bayesian probabilistic power flow have been successively introduced [8–12]. Reference [13] achieved refined reliability evaluation considering multiple failure modes, Ref. [14] conducted probabilistic modeling of hosting capacity considering source–load uncertainties, and Ref. [15] analyzed the application effect of stochastic optimal power flow from the perspective of data value. However, the above methods mainly address conventional wind–solar fluctuations and have not fully considered the synchronous degradation effect of multiple physical field parameters under extreme high temperatures.

In terms of indicator systems and voltage regulation, Ref. [16] constructed a risk assessment indicator system considering distributed renewable energy, while Ref. [17] established an optimization model for receiving-end grids considering security and stability risk assessment. At the voltage control level, Ref. [18] studied a PV output control method considering violation risk, Ref. [19] proposed a distributed model-free voltage control strategy, Ref. [20] designed a multi-timescale voltage control method, Ref. [21] analyzed the causes and countermeasures of overvoltage under high-penetration PV access, and Ref. [22] proposed a complex affine arithmetic-based power-flow algorithm considering reactive power characteristics. Most of these studies target normal operating conditions and do not cover the special condition of synchronous degradation of source–grid–load parameters under extreme heat.

In the aspect of uncertainty handling and optimal scheduling, existing research has explored different technical paths. Reference [23] proposed a fast assessment method for supply–demand imbalance risk of new power systems based on deep active learning driven by weather data. Reference [24] used data-driven robust optimization to study the intraday rolling scheduling strategy of distribution networks and microgrid-integrated energy systems, and Ref. [25] proposed a two-stage robust optimization method for microgrids considering the grid-forming capability of energy storage and multiple uncertainties of wind, PV, and load. Reference [26] constructed a robust optimal dispatch model for PV-rich power systems considering demand response and energy storage. At the multi-timescale coordination and collaborative scheduling level, Ref. [27] proposed a coordinated multi-timescale optimal regulation strategy for source–grid–load–storage of distribution networks based on Fisher period division. Reference [28] studied a cooperative peer-to-peer scheduling method of multi-microgrids considering distribution network power-flow constraints and source–load uncertainty. The above studies provide rich technical accumulation for dealing with uncertainty and multi-timescale coordination issues in power systems, but their focus is on optimal scheduling and operation control, and the refined assessment of voltage violation risk itself in distribution networks under extreme high temperature still needs to be deepened.

To address the shortcomings—that existing studies have not fully considered the synchronous coupling effects of multiple physical fields under extreme high temperatures, lack node-level refined time-series assessment, and have not quantified the sunset-driven undervoltage risk caused by the simultaneous decline of PV output, delayed temperature-sensitive load peak, and thermally increased line resistance—this paper establishes a source–grid–load electro-thermal coupling model that accounts for load thermal accumulation, transient conductor thermal inertia, temperature-dependent line impedance, and PV thermal derating. The cumulant method combined with the Cornish–Fisher expansion is used to reconstruct the nodal voltage probability distribution, and a voltage violation risk assessment system covering violation probability, violation depth, expected violation duration, and a comprehensive risk factor is constructed. The effectiveness of the proposed method is validated on the IEEE 33-bus system under a 45 °C scenario.

2. Influence Mechanism of Extreme High Temperature on Voltage Violation in Distribution Networks

Under normal weather conditions, voltage violations in distribution networks are mainly caused by fluctuations in PV and wind power or local faults, and the risk propagation path is relatively simple. Under extreme high-temperature scenarios, abnormal air temperature exerts superimposed influences on the distribution network through three physical paths: the load thermal effect, the line thermal effect, and the PV thermal effect. These effects overlap in time and accumulate along the feeder direction, significantly enhancing the low-voltage risk at terminal nodes. This section analyzes the action mechanism of extreme high temperature from the perspectives of load, network, and source, and quantifies its coupled impact on node voltage [29].

2.1. Thermal Accumulation Effect and Power Evolution of Temperature-Sensitive Loads

Under extreme high-temperature conditions, the electricity demand of air-conditioning and other temperature-sensitive loads increases significantly with temperature. However, the building envelope and indoor thermal capacity cause a delay in the release of indoor heat, so that load growth is not completely synchronized with outdoor temperature. When outdoor temperature peaks at 14:00–15:00 and begins to decline, indoor temperature remains at a high level for 1–2 h, and air conditioners continue to operate to maintain the set temperature, delaying the load peak into the evening peak period. Consecutive days of high temperature also progressively raise the building base temperature, increasing the low-voltage risk at terminal nodes.

To characterize the above effects, a temperature correction term is introduced on the basis of the baseline load, and the temperature-sensitive load power is expressed as:

$$P_{L,k}(t) = P_{L0,k}[1 + \alpha_k \Delta T_{in,k}(t)], \quad (1)$$

where $P_{L0,k}$ is the load value of node k at the baseline temperature, α_k is the load temperature sensitivity coefficient of node k, $\Delta T_{in,k}(t)$ is the effective indoor–outdoor temperature difference considering thermal inertia, obtained by solving the building heat balance equation, and its time series exhibits a significant lag and smoothing effect compared with the outdoor air temperature series.

To explicitly describe the indoor thermal inertia used in Equation (1), a first-order resistance–capacitance (RC) building thermal model is adopted for temperature-sensitive

loads. For the equivalent building group connected to node k, the indoor thermal state is described as:

$$C_{b,k}\frac{dT_{in,k}(t)}{dt} = \frac{T_a(t) - T_{in,k}(t)}{R_{b,k}} + \eta_{h,k}P_{hvac,k}(t) + Q_{int,k}(t), \quad (2)$$

where $T_{in,k}(t)$ is the equivalent indoor temperature of the building group at node k, $T_a(t)$ is the outdoor ambient temperature, $C_{b,k}$ is the equivalent building thermal capacitance, $R_{b,k}$ is the equivalent thermal resistance of the building envelope, $P_{hvac,k}(t)$ is the cooling power of the air-conditioning load, $\eta_{h,k}$ is the equivalent heat-to-electric conversion coefficient, and $Q_{int,k}(t)$ represents internal heat gain.

The indoor temperature deviation used in the temperature-sensitive load model is defined as:

$$\Delta T_{in,k}(t) = T_{in,k}(t) - T_{set,k}, \quad (3)$$

where $T_{set,k}$ is the indoor temperature setpoint. For numerical implementation, Equation (2) is discretized with the same time step as the risk assessment snapshots:

$$T_{in,k}^{n+1} = T_{in,k}^{n} + \frac{\Delta t}{C_{b,k}}\left[\frac{T_a^n - T_{in,k}^n}{R_{b,k}} + \eta_{h,k}P_{hvac,k}^n + Q_{int,k}^n\right]. \quad (4)$$

Equation (4) shows that the temperature-sensitive load at the current snapshot is not determined only by the instantaneous outdoor temperature, but also by the indoor thermal state inherited from the previous snapshot. This formulation explains the delayed load peak during the evening period under extreme high-temperature conditions.

2.2. Transient Conductor Thermal Model and Temperature-Dependent Line Impedance

The resistance of overhead lines and cable conductors varies with conductor temperature. In the original quasi-steady-state formulation, the line resistance was corrected according to the operating temperature. However, overhead conductors do not instantaneously reach the thermal steady state. Owing to the heat capacity of the conductor, the conductor temperature exhibits thermal inertia, and its dynamic evolution should be considered when the assessment time resolution is comparable to the conductor thermal time constant. Therefore, in this paper, the conductor temperature is described using a transient heat-balance equation following the thermal-rating principles and transient conductor thermal models reported in related studies [30,31].

These studies have also shown that the conductor temperature may exhibit non-negligible dynamic and spatial distribution characteristics under the combined effects of current loading and environmental heat exchange. Therefore, introducing conductor thermal inertia into the voltage risk assessment is necessary for representing the delayed variation of line resistance under extreme high-temperature conditions.

For branch l, the transient thermal balance of the conductor is expressed as:

$$m_l c_{p,l}\frac{dT_{c,l}(t)}{dt} = I_l^2(t)R_l(T_{c,l}) + q_{s,l}(t) - q_{c,l}(T_{c,l}, T_a, v_w) - q_{r,l}(T_{c,l}, T_a), \quad (5)$$

where $T_{c,l}(t)$ is the conductor temperature of branch l at time t, m_l is the conductor mass per unit length, $c_{p,l}$ is the specific heat capacity of the conductor, $I_l(t)$ is the branch current, $R_l(T_{c,l})$ is the temperature-dependent resistance, $q_{s,l}(t)$ is the solar heat gain, $q_{c,l}$ is the convective heat loss related to conductor temperature, ambient temperature T_a, and wind speed v_w, and $q_{r,l}$ is the radiative heat loss related to conductor temperature and ambient temperature.

To make the transient conductor temperature calculation reproducible, the heat-exchange terms in Equation (5) are further specified in a simplified per-unit-length form. The solar heat gain is calculated as:

$$q_{s,l}(t) = \alpha_s D_l G(t), \tag{6}$$

where α_s is the solar absorptivity of the conductor surface, D_l is the equivalent conductor diameter of branch l, and $G(t)$ is the global solar irradiance incident on the conductor.

The convective heat loss is represented by:

$$q_{c,l}(t) = \pi D_l h_c [T_{c,l}(t) - T_a(t)], \tag{7}$$

where h_c is the equivalent convective heat-transfer coefficient. In this study, h_c is estimated using the empirical relation $h_c = 5.7 + 3.8 v_w$, where v_w is the wind speed. A constant wind speed is assumed during the evening assessment period.

The radiative heat loss is calculated as:

$$q_{r,l}(t) = \pi D_l \varepsilon \sigma_{\mathrm{SB}} [(T_{c,l}(t) + 273.15)^4 - (T_a(t) + 273.15)^4], \tag{8}$$

where ε is the surface emissivity of the conductor, and σ_{SB} is the Stefan–Boltzmann constant. In Equation (8), temperatures are converted from degrees Celsius to Kelvin for the radiation calculation.

In the numerical implementation, a uniform effective conductor is adopted for all branches because the standard IEEE 33-bus test system does not provide detailed conductor surface and geometric data for each branch. If detailed conductor and meteorological data are available, D_l, α_s, ε, h_c,v_w, and $G(t)$ can be replaced by branch-specific or time-varying values without changing the proposed electro-thermal coupling framework.

In the numerical simulation, Equation (5) is treated as the governing transient thermal equation for the conductor temperature. The conductor temperature is not assigned as a prescribed steady-state value at each assessment snapshot. Instead, the net thermal-balance term, including current-induced Joule heating and weather-related heat exchange, is discretized over adjacent snapshots so that the conductor temperature is recursively updated from the previous thermal state. In this way, the conductor heat capacity and thermal memory are retained in the electro-thermal power-flow calculation.

The temperature-dependent resistance of branch l is updated as:

$$R_l(T_{c,l}) = R_{l,0}[1 + \alpha_R (T_{c,l} - T_0)], \tag{9}$$

where $R_{l,0}$ is the conductor resistance at the reference temperature T_0, and α_R is the temperature coefficient of resistance.

For numerical implementation, the transient conductor temperature is discretized over adjacent assessment snapshots. The temperature update equation is written as:

$$T_{c,l}^{n+1} = T_{c,l}^{n} + \frac{\Delta t}{m_l c_{p,l}} \left[I_l^{2,n} R_l(T_{c,l}^{n}) + q_{s,l}^{n} - q_{c,l}^{n} - q_{r,l}^{n} \right], \tag{10}$$

where $T_{c,l}^{n}$ and $T_{c,l}^{n+1}$ are the conductor temperatures of branch l at the n-th and $(n+1)$-th assessment snapshots, respectively, and Δt is the time interval between two adjacent snapshots. Equation (10) indicates that the conductor temperature at the next snapshot is not independently recalculated from an instantaneous steady-state balance but is recursively obtained from the previous thermal state. Therefore, the proposed model preserves the conductor thermal memory caused by heat capacity. The conventional algebraic thermal-

balance equation corresponds to the limiting case of Equation (5), where the temperature derivative becomes zero. In contrast, the present formulation retains the derivative term and updates $T_{c,l}$ over adjacent assessment snapshots. Since the thermal time constant of overhead conductors is generally on the order of several to tens of minutes and depends on conductor type, current level, wind condition, and solar heating, the 30 min assessment interval used in this study is comparable to the conductor thermal response scale. Therefore, the conductor temperature cannot be assumed to instantaneously reach a new steady state at each snapshot. By using Equation (10), the proposed electro-thermal model avoids the instantaneous steady-state approximation and captures the delayed response of line resistance to current and meteorological variations.

After obtaining $T_{c,l}^{n+1}$, the line resistance is updated as:

$$R_l^{n+1} = R_{l,0}\left[1 + \alpha_R(T_{c,l}^{n+1} - T_0)\right]. \tag{11}$$

The updated resistance R_l^{n+1} is then substituted into the network admittance matrix and the subsequent power-flow calculation.

The steady-state thermal balance can be regarded as a special limiting case of the transient model. When the conductor reaches thermal equilibrium, the temperature derivative in Equation (5) becomes zero, and Equation (5) degenerates into:

$$(I_l^2 R_l(T_{c,l}) + q_{s,l} - q_{c,l} - q_{r,l} = 0). \tag{12}$$

Therefore, the conventional algebraic thermal-balance model corresponds only to the steady-state limiting case of the transient formulation. In contrast, the proposed calculation retains the transient term in Equation (5) and recursively updates the conductor temperature over adjacent assessment snapshots, thereby describing the delayed response of conductor temperature and line resistance to variations in branch current and meteorological conditions.

In the simplified voltage-drop model of a single-load branch in a distribution network, the branch voltage magnitude loss is approximated as:

$$\Delta U_l \approx \frac{R_l(T_{c,l})P_l + X_l Q_l}{U_N}, \tag{13}$$

where P_l and Q_l are the active and reactive power flows through branch l, respectively, X_l is the branch reactance, and U_N is the rated voltage.

Under extreme high-temperature conditions, the increase in conductor temperature causes the line resistance to rise dynamically. When the resistances of multiple lines along a feeder path increase simultaneously, the voltage drop at downstream nodes becomes more significant. As a result, the sensitivity of terminal node voltage to source–load disturbances is enhanced. Under the same magnitude of PV output fluctuation or load disturbance, the node voltage deviation becomes larger, the variance of the node voltage distribution increases, and the left-tail probability of the voltage probability density function becomes thicker. This is the physical mechanism by which conductor thermal inertia and temperature-dependent resistance increase the risk of low-voltage violation under extreme high-temperature conditions.

2.3. Thermal Derating Characteristics of Distributed PV Output

The power generation efficiency of PV modules decreases approximately linearly as the panel temperature rises, and the corrected output power is expressed as:

$$P_{\mathrm{PV},t} = \eta_N S I_t[1 - \beta_{\mathrm{PV}}(T_{\mathrm{cell},t} - T_{\mathrm{ref}})], \tag{14}$$

where η_N is the rated conversion efficiency, S is the equivalent area of the module, I_t is the real-time irradiance, β_P is the power temperature derating coefficient, with reference to typical parameters in related studies on temperature characteristics of PV modules (this paper adopts $\beta_{PV} = 0.0045/^{\circ}\mathrm{C}$, and the derating term is expressed as $1 - \beta_{PV}(T_{cell} - T_{ref})$), and T_{ref} is the standard test temperature.

Suppression of photoelectric conversion efficiency by high temperatures will weaken the active power support capability of distributed PV under extreme operating conditions. For the feeder-end node, the decline in local support capability means that its available voltage buffering capacity is reduced during rapid load increases, thereby raising the probability of the node voltage falling below the lower safety limit.

2.4. Coupled Low-Voltage Risk Mechanism Under Source–Network–Load Degradation

Under extreme high-temperature conditions, the risk of low voltage in distribution networks is primarily caused by the superposition in time and space of three categories of degradation factors: source, network, and load. During the daytime peak high-temperature period, PV still provides a certain level of voltage support, but the load increases rapidly. After sunset in the evening, PV output drops sharply, while temperature-sensitive loads remain high due to building thermal inertia, causing the net load at the terminal node to rise rapidly.

A large number of temperature-sensitive loads at the terminal, such as inverter air conditioners, can be approximately regarded as constant power loads, and their nodal power equation is:

$$I_L = \left(\frac{P_L + jQ_L}{U_L} \right), \tag{15}$$

where I_L is the injected current phasor at the constant power load node, U_L is the node voltage phasor, while P_L and Q_L are the active and reactive power demands, respectively, required to maintain the rated cooling output under extreme high temperatures.

The constant power representation is used here as an aggregate approximation for temperature-sensitive cooling loads during the short-term risk assessment window. It is mainly intended to describe inverter air conditioners and electronically controlled cooling devices that tend to maintain their cooling output within the normal voltage range. Under this approximation, a voltage decrease can increase the current demand, which further enlarges the feeder voltage drop and provides a conservative estimate of low-voltage risk.

This assumption does not imply that all air-conditioning loads behave as ideal constant power devices. In practice, temperature-sensitive loads may include impedance, current, and constant power components, and their operation may also be influenced by low-voltage protection or local control strategies. Therefore, the constant power model should be interpreted as a conservative operating assumption for the present risk assessment. ZIP-type and protection-constrained load models will be considered in future work.

Under the constant power load assumption, when the node voltage drops due to weakened local support and heavy transmission loading, the load draws a larger current in order to maintain constant output power. This increased current then flows through the lines that are already in a high-temperature, high-resistance state, further amplifying the line voltage drop and thereby aggravating the local low-voltage risk. This process is also accompanied by significant uncertainties. Local cloud variations can cause PV output fluctuations, and temperature forecast errors can also cause the load level to deviate from its predicted value. The superposition of multi-source stochastic disturbances leads to increased node voltage volatility, thereby raising the probability of low-voltage limit violation. Relying solely on traditional deterministic verification methods to judge "whether a limit is violated" fails to reflect the true risk level when the node voltage approaches the

safety boundary under extreme high-temperature scenarios. It is necessary to perform a continuous quantitative assessment from both the probability and severity perspectives.

3. Risk Assessment Indicators for Node Voltage Limit Violation Under Extreme High Temperature

Under extreme high-temperature conditions, the deterministic characteristics of the distribution network operating state undergo significant changes, and the influence of source-side and load-side uncertainties on node voltage intensifies. The node voltage exhibits stochastic characteristics along with temperature deviations, PV output, and load fluctuations. The traditional binary limit violation judgment (violation/no violation) is insufficient to fully characterize the low-voltage risk; therefore, it is necessary to conduct continuous quantification of the node voltage from two dimensions: probability and severity.

3.1. Node Voltage Limit Violation Probability Considering Multi-Source Uncertainties

Under extreme high-temperature conditions, multi-source stochastic disturbances, such as ambient temperature forecast errors and local irradiance fluctuations, propagate through the distribution network, causing the node voltage to exhibit a continuous random distribution, which can be described by a probability density function (PDF).

Let the voltage magnitude at a node be a random variable. Through a probabilistic power-flow algorithm that accounts for source–load forecast errors, the probability density function (PDF) of each node voltage under extreme weather scenarios can be obtained, denoted as $f(V_i)$. For a distribution network with high penetration of PV, the sunset-driven undervoltage risk under extreme high temperature primarily manifests as a deep low-voltage risk caused by the weakening of local voltage support capability during the evening peak. It should be noted that this term does not refer to classical voltage collapse in the voltage-stability sense, but to a time-dependent undervoltage risk induced by PV output decline, delayed thermal load demand, and thermally increased feeder impedance. The probability that the node voltage falls below the system's predetermined lower safety limit $V_{\min}$ can be expressed as:

$$P_{v,i} = P(V_i < V_{\min}) = \int_0^{V_{\min}} f(V_i) dV_i, \tag{16}$$

where $P_{v,i}$ is the voltage limit violation probability of node i and $V_{\min}$ is the specified lower safety limit of the node voltage. This indicator quantifies the probability that the node voltage falls below the safety lower limit under multi-source stochastic disturbances. In this paper, the soft lower safety limit is taken as 0.95 p.u.

3.2. Node Voltage Limit Violation Severity Based on Risk-Preference Utility Function

This indicator quantifies the nonlinear consequence severity when the node voltage falls below the safety lower limit. In this paper, the soft lower safety limit is taken as 0.95 p.u. Deep low voltage may cause abnormal operation of variable-frequency constant power equipment and amplify local reactive power deficits and line voltage drops. Therefore, the risk consequence does not increase linearly with the voltage deviation depth, and a nonlinear risk-preference utility function is introduced to characterize this effect. The node voltage limit violation severity is expressed by a risk-preference utility function, which is used to quantify the nonlinear increase of risk with the depth of violation as the voltage

deviates from the safety lower limit. Define the voltage drop deviation $\omega_i = V_{\min} - V_i$ (when $V_{\min} > V_i$), and its severity utility function can be expressed in exponential form:

$$S(\omega_i) = \gamma(e^{\omega_i} - 1), \tag{17}$$

where ω_i is the low-voltage deviation measured in p.u., and $S(\omega_i)$ is a dimensionless severity utility. The proposed metric is not a purely linear or quadratic penalty. For small deviations, the Taylor expansion of the exponential function gives $S(\omega_i) \approx \gamma\omega_i + \frac{\gamma}{2}\omega_i^2 + \ldots$, which indicates that shallow violations are mainly weighted by the first-order term, whereas deeper violations receive an additional convex penalty.

In this study, $\gamma = 1/(e-1) \approx 0.582$, so that $S(1) = 1$ when the normalized severity index is $\omega_i = 1$. This normalization gives a clear reference scale for comparing low-voltage events. Values reported as $100S(\omega_i)$ in figures and tables are, therefore, scaled dimensionless severity utilities, rather than physical voltage deviation percentages. Consequently, a displayed value greater than 100 does not imply that the physical voltage violation depth exceeds 100%, it only indicates that the event is more severe than the selected reference level.

The exponential form is adopted because the operational consequence of low voltage usually increases faster as the voltage moves further below the 0.95 p.u. safety boundary. Under deeper voltage depression, constant power and variable-frequency loads may draw larger currents, reactive power shortage may be amplified, and feeder-end voltage drops may become more serious. The influence of the selected γ value on the main conclusions is examined in Section 5.5.

3.3. System-Level Comprehensive Risk Indicator Coupled with Multiphysics Boundaries

This paper integrates the node voltage probability density function with the severity utility function to construct a comprehensive node voltage limit violation risk indicator. The calculation model of the comprehensive voltage limit violation risk indicator $R_{v,i}$ for node i under the extreme high-temperature forecast snapshot is constructed as follows:

$$R_{v,i} = \int_0^{V_{\min}} f(V_i) \cdot S(V_{\min} - V_i) dV_i, \tag{18}$$

where $R_{v,i}$ is the comprehensive voltage limit violation risk assessment indicator for node i under extreme high-temperature scenarios, $S(V_{\min} - V_i)$ is the node voltage drop severity utility function that satisfies the properties of a nonlinear convex function, and $f(V_i)$ is the probability density function of the voltage magnitude at node i, which accounts for multi-source uncertainties from weather and source–load and is obtained through probabilistic power-flow calculation.

The comprehensive risk factor $R_{v,i}$ is a dimensionless expected severity utility obtained by integrating the voltage probability density function and the severity utility function over the low-voltage violation region. It is not expressed in p.u. or in percent. The voltage deviation itself is measured in p.u., the violation probability is dimensionless, and the physical violation depth in Equation (24) can be expressed as a percentage, while the comprehensive risk factor in Equation (18) remains a dimensionless expected utility value.

The system average risk factor and the maximum node risk factor are used to quantify the overall network risk level and identify weak nodes, respectively. When the indicator exceeds the preset threshold, the system already faces a high-voltage limit violation risk under extreme high temperature, defined as follows:

$$R_{sys}(t) = \frac{1}{N_L} \sum_{i \in \Omega_L} R_i(t), \tag{19}$$

$$R_{\max}(t) = \max_{i \in \Omega_L} R_i(t), \tag{20}$$

where $R_{sys}(t)$ is the system average risk factor, $R_i(t)$ is the risk factor of node i, Ω_L is the set of load nodes, and N_L is the number of load nodes.

In addition to the system average expected severity utility in Equation (19), an engineering system composite risk factor is further introduced for cross-scenario comparison in the simulation section. This factor jointly considers the system average violation probability and the system average scaled severity utility.

The system average low-voltage violation probability is defined as:

$$\overline{P}_{vio}(t) = \frac{1}{N_L} \sum i \in \Omega_L P_{v,i}^{\text{low}}(t). \tag{21}$$

The system average conditional severity utility is defined as:

$$\overline{S}_{sev}(t) = \frac{1}{N_L} \sum i \in \Omega_L \overline{S}_i(t), \tag{22}$$

where $\overline{S}_i(t)$ denotes the conditional average dimensionless severity utility of node i under the low-voltage violation condition. When $P_{v,i}^{low}(t) = 0$, $\overline{S}_i(t)$ is set to zero.

The engineering system composite risk factor is then defined as:

$$w_p \frac{\overline{P}_{vio}(t)}{P_{norm}} + w_s \frac{\overline{S}_{sev}(t)}{S_{norm}}, \tag{23}$$

where $F_{\text{sys}}(t)$ is the engineering system composite risk factor, w_p and w_s are the weights of violation probability and severity, respectively, with $w_p + w_s = 1$, while P_{norm} and S_{norm} are normalization constants for probability and severity. In this study, $w_p = w_s = 0.5$, the probability normalization constant is set as $P_{\text{norm}} = 1$, and the severity normalization constant is set according to the maximum displayed severity utility, $S_{\text{norm}} = \gamma(e^{\omega_{\max}} - 1)$. In the numerical presentation, the violation probability is reported in percentage form, while the severity utility is reported as a dimensionless value scaled by 100 for display. The engineering system composite risk factor remains dimensionless.

3.4. Physical Voltage Violation Depth and Expected Duration Indicators

The physical voltage violation depth is used to characterize the relative deviation magnitude when the node voltage falls below the safety lower limit. This indicator is different from the dimensionless severity utility defined in Equation (17) because it directly measures the voltage deviation ratio and can be expressed as a percentage. For node i at time t with voltage magnitude $V_i(t)$, its physical low-voltage violation depth is defined as:

$$\eta_i(t) = \max\left\{0, \frac{V_{\min} - V_i(t)}{V_{\min}}\right\} \times 100\%, \tag{24}$$

where $\eta_i(t)$ is the physical low-voltage depth of node i at time t, and $V_{\min}$ is the safety lower limit of the node voltage. When $V_i(t) \geq V_{\min}$, the node voltage is within the safety range, $\eta_i(t) = 0$; when $V_i(t) < V_{\min}$, $\eta_i(t)$ represents the ratio of the drop of the node voltage relative to the safety lower limit.

In probabilistic power-flow calculation, the node voltage is a continuous random variable. Let the probability density function of the voltage at node i at time t be $f_i(v, t)$, then its low-voltage limit violation probability is:

$$P_i^{low}(t) = \int_{-\infty}^{V_{\min}} f_i(v, t) dv. \tag{25}$$

On this basis, the conditional average physical voltage violation depth of node i at time t is defined as:

$$\overline{\eta}_i(t) = \frac{\int_{-\infty}^{V_{\min}} \frac{V_{\min} - v}{V_{\min}} f_i(v,t)dv}{P_i^{low}(t)} \times 100\%, \tag{26}$$

where $\overline{\eta}_i(t)$ is the conditional average physical voltage violation depth of node i under the condition of low-voltage violation. When $P_i^{\text{low}}(t) = 0$, $\overline{\eta}_i(t) = 0$. This indicator reflects the average physical voltage deviation ratio by which the node voltage falls below the safety boundary under violation conditions, and it is different from the dimensionless severity utility $S(\omega_i)$ defined in Equation (17).

To quantify the evolution characteristics of low-voltage limit violation over time, the expected violation duration indicator of a node within the evaluation period is introduced, and the calculation formula is:

$$T_i^{\text{exp}} = \sum_{t \in T} P_i^{low}(t)\Delta t, \tag{27}$$

where T_i^{exp} is the expected violation duration of node i, Δt is the time interval between adjacent calculation snapshots, and T is the set of risk assessment snapshots. In the discrete implementation, T_i^{exp} represents the probability-weighted accumulated violation duration over all assessment snapshots rather than the clock time difference between the first and last snapshot labels.

At the system level, the overall limit violation level can be further described by the average value of the indicators of each node in the load node set:

$$\overline{\eta}_{sys}(t) = \frac{1}{N_L} \sum_{i \in \Omega_L} \overline{\eta}_i(t), \tag{28}$$

$$T_{sys}^{\text{exp}} = \frac{1}{N_L} \sum_{i \in \Omega_L} T_i^{\text{exp}}, \tag{29}$$

where $\overline{\eta}_{sys}(t)$ is the system average physical voltage violation depth, T_{sys}^{exp} is the system average expected violation duration, Ω_L is the set of load nodes, and N_L is the number of load nodes. The above indicators quantify the physical low-voltage violation from two aspects, namely, the voltage deviation ratio and the expected violation duration, providing an evaluation basis for subsequent weak node identification and risk period analysis.

4. Risk Assessment Algorithm and Process for Voltage Limit Violation in Distribution Networks Under Extreme High Temperature

The calculation of node voltage limit violation risk depends on the probability distribution of node voltage. Since the Monte Carlo method entails a heavy computational burden in multi-node systems, this paper adopts the cumulant method combined with the Cornish–Fisher expansion to efficiently solve the probabilistic power flow considering parameter degradation under extreme high temperature.

4.1. Unified Multiplicative Uncertainty Modeling and Cumulant Acquisition Under Extreme High Temperature

Under extreme high-temperature meteorological conditions, ambient temperature forecast deviations and local micro-meteorological disturbances can cause significant fluctuations in temperature-sensitive loads and distributed PV output. To maintain consistency between the probabilistic formulation and the simulation settings, this paper adopts a

unified multiplicative uncertainty model for both load and PV output. The active and reactive injected powers at node i are expressed as:

$$P_i = P_{i,0}^{\mathrm{th}} \xi_{P,i}, \tag{30}$$

$$Q_i = Q_{i,0}^{\mathrm{th}} \xi_{Q,i}, \tag{31}$$

where $P_{i,0}^{\mathrm{th}}$ and $Q_{i,0}^{\mathrm{th}}$ are the thermally corrected expected active and reactive powers at node i, respectively, while $\xi_{P,i}$ and $\xi_{Q,i}$ are multiplicative random factors describing source–load uncertainty.

For temperature-sensitive loads, the random multiplier is modeled by a Gamma distribution to ensure non-negative load samples. Its mean is normalized to 1, so that the deterministic thermally corrected load remains the expected value. For distributed PV output, the random multiplier is modeled by a Beta distribution because PV power is naturally bounded between zero and the available irradiance-dependent output. For the Gamma-distributed load multiplier, the shape and scale parameters are determined from the normalized mean and coefficient of variation. Since $E[\xi_L] = 1$, the parameters are set as $k_L = 1/c_L^2$ and $\theta_L = c_L^2$, where c_L is the coefficient of variation of the load multiplier. For the PV uncertainty model, the bounded normalized PV output ratio is modeled by a Beta distribution, and the mapping from the normalized mean and coefficient of variation to the distribution parameters is explicitly given as follows. Let $Z_{\mathrm{PV},i,t}$ denote the normalized PV output ratio at node i and assessment snapshot t, where $0 < Z_{\mathrm{PV},i,t} < 1$. It is assumed to follow:

$$Z_{\mathrm{PV},i,t} \sim \mathrm{Beta}(\alpha_{\mathrm{PV},i,t}, \beta_{\mathrm{PV},i,t}). \tag{32}$$

The normalized mean and coefficient of variation are denoted by $\mu_{\mathrm{PV},i,t}$ and c_{PV}, respectively. Therefore, the variance of the normalized PV output ratio is:

$$\sigma_{\mathrm{PV},i,t}^2 = (c_{\mathrm{PV}} \mu_{\mathrm{PV},i,t})^2. \tag{33}$$

According to the mean and variance relationships of the Beta distribution, the two shape parameters are obtained as:

$$\alpha_{\mathrm{PV},i,t} = \mu_{\mathrm{PV},i,t} \left[\frac{\mu_{\mathrm{PV},i,t}(1 - \mu_{\mathrm{PV},i,t})}{\sigma_{\mathrm{PV},i,t}^2} - 1 \right], \tag{34}$$

$$\beta_{\mathrm{PV},i,t} = (1 - \mu_{\mathrm{PV},i,t}) \left[\frac{\mu_{\mathrm{PV},i,t}(1 - \mu_{\mathrm{PV},i,t})}{\sigma_{\mathrm{PV},i,t}^2} - 1 \right]. \tag{35}$$

The feasibility conditions are $0 < \mu_{\mathrm{PV},i,t} < 1$ and $0 < \sigma_{\mathrm{PV},i,t}^2 < \mu_{\mathrm{PV},i,t}(1 - \mu_{\mathrm{PV},i,t})$. In the multiplicative uncertainty formulation used in Equations (30) and (31), the mean-1 PV random factor is further obtained by:

$$\xi_{\mathrm{PV},i,t} = \frac{Z_{\mathrm{PV},i,t}}{\mu_{\mathrm{PV},i,t}}, \tag{36}$$

so that $E[\xi_{\mathrm{PV},i,t}] = 1$, while its coefficient of variation remains c_{PV}. Therefore, the thermally corrected PV output remains the expected value in the probabilistic power-flow calculation, and the uncertainty magnitude is explicitly controlled by the coefficient of variation.

Therefore, the uncertainty model used in the cumulant calculation is consistent with the simulation setup in Section 5.

In this study, random multipliers at different nodes and different assessment snapshots are assumed to be independent. The correlation among ambient temperature, load level,

and PV derating is reflected through the deterministic electro-thermal correction model, while the residual stochastic forecast errors are treated as independent perturbations. The uncertainty magnitude is controlled by the coefficient of variation of the corresponding random multipliers.

To enable efficient linear operations on random variables, cumulants are introduced to characterize their statistical features. Let the multiplicative random factor ξ, representing $\xi_{P,i}$ or $\xi_{Q,i}$, have cumulants of various orders denoted by $\kappa_r(\xi)$. The cumulants of the injected power can then be obtained by scaling the cumulants of the random factor. For example, for $P_i = P_{i,0}^{\mathrm{th}}\xi_{P,i}$, the r-th-order cumulant is:

$$\kappa_r(P_i) = \left(P_{i,0}^{\mathrm{th}}\right)^r \kappa_r(\xi_{P,i}). \tag{37}$$

Similarly, the cumulants of Q_i can be obtained from $\xi_{Q,i}$. In this way, the probability distributions of source–load uncertainties are converted into cumulant sequences of nodal injected power, which serve as the inputs of the probabilistic power-flow calculation.

4.2. Probabilistic Power-Flow Calculation of Distribution Networks Considering Multiphysics Coupling

Under extreme high-temperature scenarios, the line parameters of the distribution network change significantly due to conductor temperature rise. The thermally corrected line resistance, thermally accumulated load, and PV thermal derating are incorporated into the nonlinear AC power-flow equation. The deterministic reference operating point under extreme high-temperature degradation conditions is expressed as:

$$W_0 = h\big(V_0; Y(R_l(T_{c,l})), P_L(T_a), P_{PV}(T_{pv})\big), \tag{38}$$

where W_0 is the injected power phasor at the reference operating point, $h(\cdot)$ is the nonlinear AC power-flow equation, V_0 is the deterministic reference operating point voltage vector, $Y(R_l(T_{c,l}))$ is the network admittance matrix updated according to the temperature-dependent line resistance, $P_L(T_a)$ is the thermally corrected load power, and $P_{PV}(T_{pv})$ is the PV output corrected by the module temperature.

At each assessment snapshot, the deterministic reference operating point U_0 is obtained through an electro-thermal iterative procedure. First, the AC power flow is solved using the conductor resistance inherited from the previous thermal state. Then, the branch current I_l is calculated and substituted into the transient conductor heat-balance equation. Next, the conductor temperature $T_{c,l}$ and the corresponding resistance $R_l(T_{c,l})$ are updated. Finally, the network admittance matrix is rebuilt based on the updated resistance, and the AC power flow is solved again.

The electro-thermal iteration is repeated until both the conductor temperature and nodal voltage convergence criteria are satisfied:

$$\max_l \left| T_{c,l}^{r+1} - T_{c,l}^{r} \right| < \varepsilon_T, \tag{39}$$

$$\max_i \left| V_i^{r+1} - V_i^{r} \right| < \varepsilon_V, \tag{40}$$

where r is the electro-thermal iteration index, ε_T is the conductor temperature convergence tolerance, and ε_V is the nodal voltage convergence tolerance.

After the electro-thermal iteration converges, the corrected conductor resistance is used to construct the admittance matrix and calculate the voltage sensitivity matrix. Therefore, the conductor temperature is no longer treated as an instantaneous steady-state value at each time step. Instead, the conductor thermal state is inherited and updated between

adjacent assessment snapshots, so that the resistance used in the probabilistic power-flow calculation reflects the transient electro-thermal state of the distribution line.

To avoid excessive computational burden in stochastic simulations, the proposed method does not update the admittance matrix or Jacobian matrix for every random sample. Instead, the electro-thermal iteration is performed only at the deterministic reference operating point of each assessment snapshot. After the conductor temperature and temperature-dependent resistance converge, the corrected admittance matrix is constructed once, and the voltage sensitivity matrix is obtained around this thermally corrected operating point.

For Monte Carlo or LHS-based electro-thermal probabilistic power flow, if N_s random samples are used, the power-flow and electro-thermal iteration need to be repeated for each sample. The approximate computational burden can be expressed as:

$$C_{\mathrm{MC}} \approx N_t N_s K_{\mathrm{th}} C_{\mathrm{PF}}(N), \tag{41}$$

where N_t is the number of assessment snapshots, N_s is the number of stochastic samples, K_{th} is the average number of electro-thermal iterations, and $C_{\mathrm{PF}}(N)$ is the computational cost of one deterministic power-flow solution for a network with N nodes.

In contrast, in the proposed cumulant-based method, the electro-thermal iteration is performed only once for each assessment snapshot to obtain the thermally corrected reference operating point. The stochastic propagation of source–load uncertainty is then completed analytically through the voltage sensitivity matrix and cumulants. Therefore, the computational burden of the proposed method can be approximated as:

$$C_{\mathrm{proposed}} \approx N_t K_{\mathrm{th}} C_{\mathrm{PF}}(N) + N_t C_{\mathrm{cum}}(N), \tag{42}$$

where $C_{\mathrm{cum}}(N)$ represents the computational cost of cumulant propagation and Cornish–Fisher reconstruction. Since $C_{\mathrm{cum}}(N)$ mainly involves matrix operations based on the voltage sensitivity matrix, it is usually much smaller than repeatedly solving thousands of nonlinear electro-thermal power-flow problems.

The computational saving ratio relative to sample-based electro-thermal probabilistic power flow can be approximately expressed as:

$$\eta = \frac{C_{\mathrm{MC}}}{C_{\mathrm{proposed}}} \approx \frac{N_t N_s K_{\mathrm{th}} C_{\mathrm{PF}}(N)}{N_t K_{\mathrm{th}} C_{\mathrm{PF}}(N) + N_t C_{\mathrm{cum}}(N)}. \tag{43}$$

When N_s is large, the proposed method can significantly reduce the number of repeated power-flow calculations. Therefore, the main computational cost of the proposed method is related to the number of assessment snapshots and electro-thermal iterations, rather than the number of stochastic samples. This feature improves the scalability of the proposed multiphysics risk assessment framework for distribution networks with a large number of uncertain source–load scenarios.

At the reference operating point V_0, the node voltage micro-increment ΔV and the injected power micro-increment ΔW satisfy the following approximate linear mapping relationship:

$$\Delta V = S_0 \Delta W, \tag{44}$$

where S_0 is the sensitivity matrix of the distribution network voltage to power disturbances.

Line overloading and high temperature with high resistance increase some elements of the sensitivity matrix. Therefore, even if the source–load prediction error is small, under high-temperature and high-resistance conditions it may cause more significant node voltage fluctuations.

According to the homogeneous additivity of semi-invariants of independent random variables, the k-st-order semi-invariant $\gamma_V^{(k)}$ of the node voltage can be obtained through matrix operations between the sensitivity matrix and the k-rd-order semi-invariant $\gamma_W^{(k)}$ of the injected power:

$$\gamma_V^{(k)} = (S_0)^{(k)} \gamma_W^{(k)}, \tag{45}$$

where $\gamma_V^{(k)}$ is the k-nd-order semi-invariant vector of the node voltage magnitudes across the entire network, and $(S_0)^{(k)}$ denotes the Hadamard product matrix obtained by raising each element of the deteriorated sensitivity matrix S_0 to the k-th power.

4.3. Reconstruction of Node Voltage Probability Density Based on Cornish–Fisher Expansion

After obtaining the high-order cumulants of the node voltage, the continuous probability density function and cumulative distribution function need to be reconstructed to support subsequent risk indicator calculation. In the numerical implementation of this study, voltage cumulants up to the fifth order are retained. The first- and second-order cumulants describe the mean value and variance of the voltage distribution, the third- and fourth-order cumulants describe its skewness and kurtosis, and the fifth-order cumulant is used to further improve the approximation of tail behavior.

Since source–load fluctuations under extreme high-temperature conditions may cause the nodal voltage to exhibit a weakly non-Gaussian and skewed distribution, the Cornish–Fisher expansion is introduced to approximately reconstruct the voltage distribution and characterize the low-voltage tail probability when the voltage approaches the safety boundary. This treatment is suitable for voltage distributions that are continuous, single-peaked, and not strongly truncated. If the voltage distribution becomes heavily tailed, multimodal, or truncated by discrete control actions or protection operations, the approximation accuracy of the Cornish–Fisher expansion may deteriorate, and additional Monte Carlo verification or non-parametric density estimation should be employed.

Let the standardized voltage variable of node i be $\widetilde{V}_i$, and its expression is:

$$\widetilde{V}_i = \frac{V_i - \mu_{v,i}}{\sigma_{v,i}}, \tag{46}$$

where $\mu_{v,i}$ and $\sigma_{v,i}$ are the expected value and standard deviation of the node voltage, respectively, obtained through high-order cumulant mapping.

Based on the Cornish–Fisher expansion, the quantile $z(\alpha)$ of the standard normal distribution can be corrected to the approximate quantile $x(\alpha)$ of the true voltage distribution:

$$\begin{aligned} x(\alpha) \approx \; & z(\alpha) + \tfrac{\lambda_3}{6}\left(z^2(\alpha) - 1\right) + \\ & \tfrac{\lambda_4}{24}\left(z^3(\alpha) - 3z(\alpha)\right) - \\ & \tfrac{\lambda_3^2}{36}\left(2z^3(\alpha) - 5z(\alpha)\right) + \ldots \end{aligned}, \tag{47}$$

where the standardized cumulant coefficients are calculated from the high-order voltage cumulants. In the displayed Cornish–Fisher correction, the skewness and kurtosis terms are explicitly shown as the dominant non-Gaussian correction terms, while the fifth-order cumulant is retained in the numerical reconstruction to improve the approximation of the distribution tail.

Based on the above expansion, the cumulative distribution function $F(V_i)$ of the node voltage can be approximately reconstructed. For a given safety lower limit threshold $V_{\min}$, the corresponding cumulative distribution function value $F(V_{\min})$ can directly characterize the low-voltage limit violation probability measure of that node. Furthermore, by differen-

tiating the cumulative distribution function, the continuous probability density function $f(V_i)$ of the node voltage can be extracted, expressed as:

$$f(V_i) = \frac{dF(V_i)}{dV_i}, \tag{48}$$

where $f(V_i)$ is the analytical function obtained from reconstruction, and the limit violation probability is used for the subsequent risk indicator calculation.

4.4. Comprehensive Risk Assessment Process for Voltage Limit Violation in Distribution Networks Under Extreme High Temperature

Combined with the above models and algorithms, the comprehensive risk assessment process for voltage limit violation in distribution networks under extreme high-temperature scenarios is shown in Figure 1, with the main steps as follows:

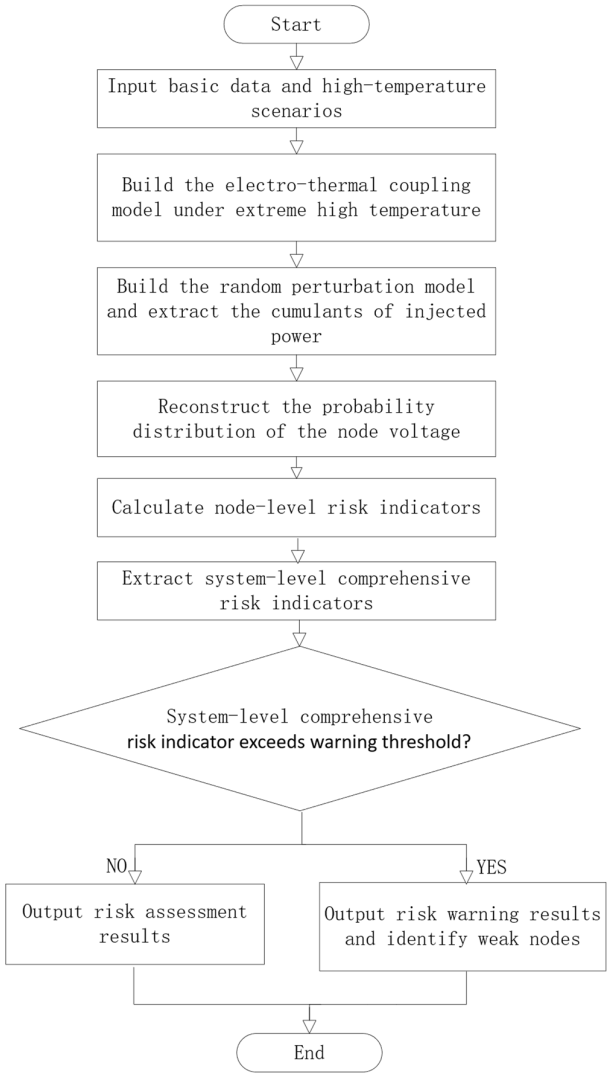


Figure 1. Comprehensive voltage violation risk assessment flow under extreme heat.

(1) Input distribution network topology parameters, node load data, distributed PV parameters, and extreme high-temperature meteorological data, establish an electro-thermal coupling model that accounts for load thermal accumulation, transient conductor thermal inertia, temperature-dependent line impedance, and PV thermal derating, and construct a source–load stochastic disturbance model.

(2) Solve the deterministic electro-thermal base power flow of the system under extreme high-temperature scenarios. At each assessment snapshot, the conductor temperature, temperature-dependent resistance, admittance matrix, and nodal voltage are iteratively updated until the electro-thermal convergence criteria are satisfied. After convergence, the thermally corrected reference operating point and voltage sensitivity matrix are obtained. The statistical characteristics of injected power stochastic disturbances are then combined to calculate the cumulants of nodal injected power and nodal voltage.

(3) Reconstruct the probability density function and cumulative distribution function of each node voltage using the Cornish–Fisher expansion; on this basis, calculate the node voltage limit violation probability, physical violation depth, dimensionless severity utility, and expected violation duration, and further derive the node-level and system-level comprehensive risk indicators.

(4) Compare the system-level comprehensive risk indicator with the preset threshold. When the indicator exceeds the threshold, high-risk periods and weak nodes can be identified, and risk warnings can be output to provide a quantitative basis for dispatch optimization.

5. Simulation Analysis

This paper uses the IEEE 33-bus distribution test system to validate the proposed voltage limit violation risk assessment model under extreme high temperature, and the simulation is performed on the MATLAB R2024a platform. High-proportion distributed PV clusters are connected at buses 7, 14, and 23, with installed capacities of 0.80 MW, 0.70 MW, and 0.70 MW, respectively. Referring to common practices in probabilistic power flow and renewable energy uncertainty modeling, the load random multiplier is described by a Gamma distribution to ensure non-negative load random samples, while the PV output random multiplier is described by a Beta distribution to reflect its bounded random characteristics. Specifically, both load and PV uncertainties are represented as multiplicative random factors rather than additive forecast errors. The mean values of the random multipliers are normalized to 1, so that the deterministic thermally corrected operating point represents the expected operating condition. The coefficients of variation of the load and PV random multipliers are specified separately for the conventional parameter scenario and the thermally corrected scenario below. Unless otherwise stated, the random factors at different buses and different time snapshots are assumed to be independent. The deterministic dependence of load and PV output on ambient temperature and irradiance is already captured by the electro-thermal correction model, and the stochastic factors represent the residual forecast uncertainty. To analyze the impact of parameter variations on the voltage limit violation risk of the distribution network under high-temperature conditions, this paper sets up a conventional parameter scenario and a thermally corrected scenario at an ambient temperature of 45 °C for comparison. The conventional parameter scenario only considers the external high-temperature environment input without further accounting for temperature-related parameter corrections, such as load thermal accumulation, line impedance temperature rise, and PV thermal derating, whereas the thermally corrected scenario simultaneously accounts for the above influencing factors. The structure of the IEEE 33-bus system is shown in Figure 2. The IEEE 33-bus system is used in this study to verify the physical mechanism of source–grid–load electro-thermal coupling and the effectiveness of the proposed voltage violation risk indices. The scalability of the algorithm is further discussed through computational complexity analysis, rather than by claiming that the 33-bus case alone represents large-scale distribution systems.

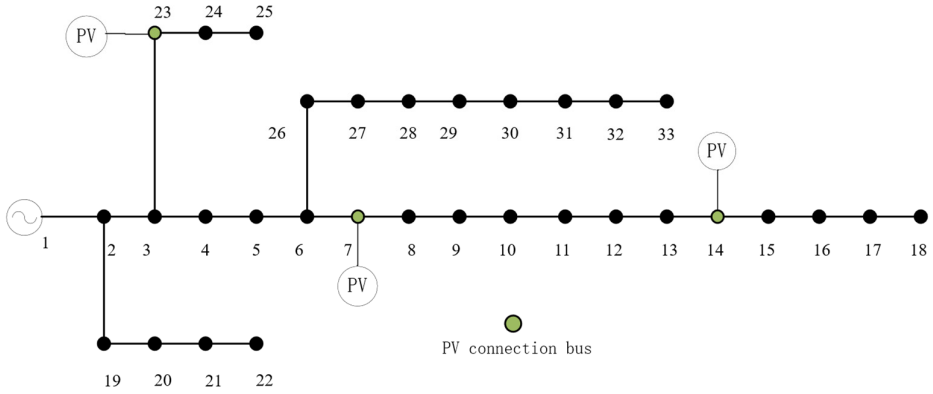


Figure 2. IEEE 33-node system wiring diagram.

The assessment period covers the sunset and evening peak interval from 17:00 to 20:30. Eight assessment snapshots are considered, namely, 17:00, 17:30, 18:00, 18:30, 19:00, 19:30, 20:00, and 20:30, with a time resolution of 30 min. In the expected duration calculation, each snapshot is assigned a 30 min duration weight. Therefore, the maximum possible accumulated violation duration over the eight-snapshot assessment period is ($8 \times 30 = 240$) min. The extreme high-temperature condition is represented by an ambient temperature of 45 °C, and the normalized irradiance profile during the sunset period is [0.95, 0.88, 0.78, 0.65, 0.50, 0.35, 0.20, 0.08] p.u. Distributed PV units are connected at buses 7, 14, and 23, with installed capacities of 0.80 MW, 0.70 MW, and 0.70 MW, respectively. In the conventional parameter scenario, the coefficients of variation of the load and PV random multipliers are 0.08 and 0.15, respectively, and in the thermally corrected scenario, they are 0.10 and 0.16, respectively. To improve the reproducibility of the source–network–load electro-thermal coupling simulation, the main numerical parameters that are not fully specified in the preceding text are summarized in Table 1.

Table 1. Main numerical parameters used in the electro-thermal and probabilistic calculations.

Category	Parameter	Value/Assumption
Load thermal model	Load thermal time constant	2.0 h
Load thermal model	Initial load thermal state	38 °C
Load thermal model	Temperature sensitivity coefficient	0.18
Load thermal model	Heat accumulation coefficient	0.06
PV thermal model	PV cell thermal inertia time constant	1.5 h
PV thermal model	Initial PV cell temperature	55 °C
PV thermal model	PV temperature derating coefficient	0.0045 $°C^{-1}$
Line thermal model	Line thermal inertia time constant	1.5 h
Line thermal model	Initial conductor temperature	45 °C
Line thermal model	Resistance temperature coefficient	0.00403 $°C^{-1}$
Line thermal model	Effective conductor diameter	0.01 m
Line thermal model	Solar absorptivity of conductor surface	0.5
Line thermal model	Surface emissivity of conductor	0.5
Line thermal model	Wind speed during assessment period	1.0 m/s
Line thermal model	Equivalent convective heat-transfer coefficient	9.5 $W/(m^2 \cdot K)$
Line thermal model	Stefan–Boltzmann constant	5.67×10^{-8} $W/(m^2 \cdot K^4)$
Line thermal model	Solar irradiance for conductor heat gain	Normalized irradiance profile × 1000 W/m^2
Uncertainty model	Load random multiplier	Gamma distribution
Uncertainty model	Normalized PV output ratio	Beta distribution
Uncertainty magnitude	Load coefficient of variation, conventional/thermally corrected	0.08/0.10
Uncertainty magnitude	PV coefficient of variation, conventional/thermally corrected	0.15/0.16
Probabilistic validation	Monte Carlo sample size	10,000
Cornish–Fisher reconstruction	Retained cumulant order	Up to the fifth order

Note: The Beta distribution parameters of the normalized PV output ratio are calculated from the normalized mean and coefficient of variation according to Equations (32)–(35). The mean-1 PV multiplicative random factor used in the probabilistic power-flow calculation is then obtained by scaling according to Equation (36).

5.1. Analysis of Evolution Characteristics of Source–Network–Load Physical Quantities Under Multiphysics Coupling

Figures 3–5 are generated using the input profiles and thermal parameters listed in Table 1. Figure 3 is obtained from the transient conductor thermal model and temperature-dependent resistance correction, Figure 4 is obtained from the first-order RC building thermal model and temperature-sensitive load correction, and Figure 5 is obtained from the irradiance profile and PV thermal derating model.

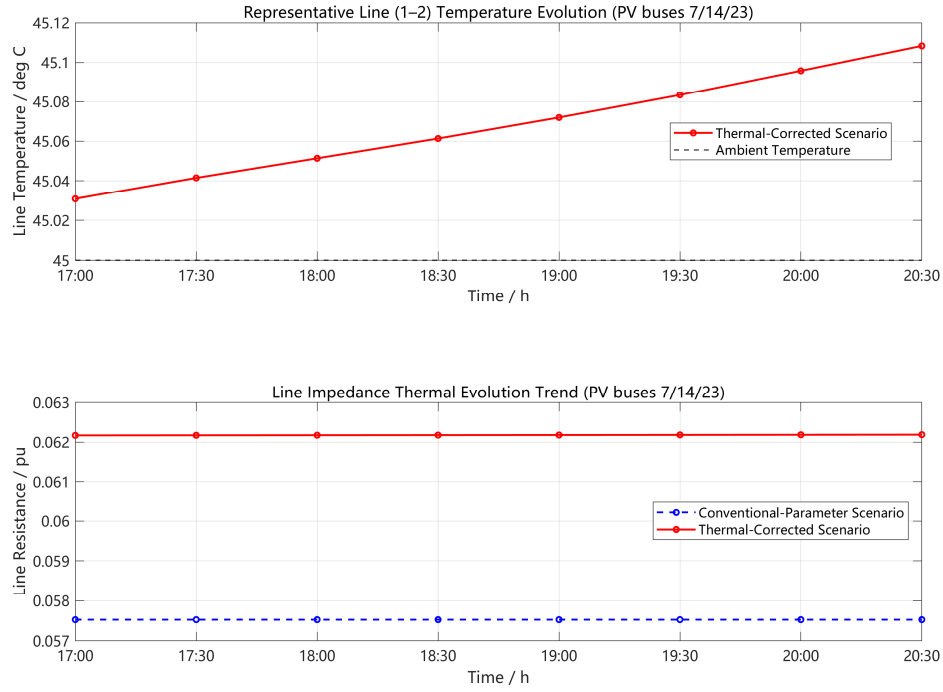


Figure 3. Thermal evolution trend of line impedance.

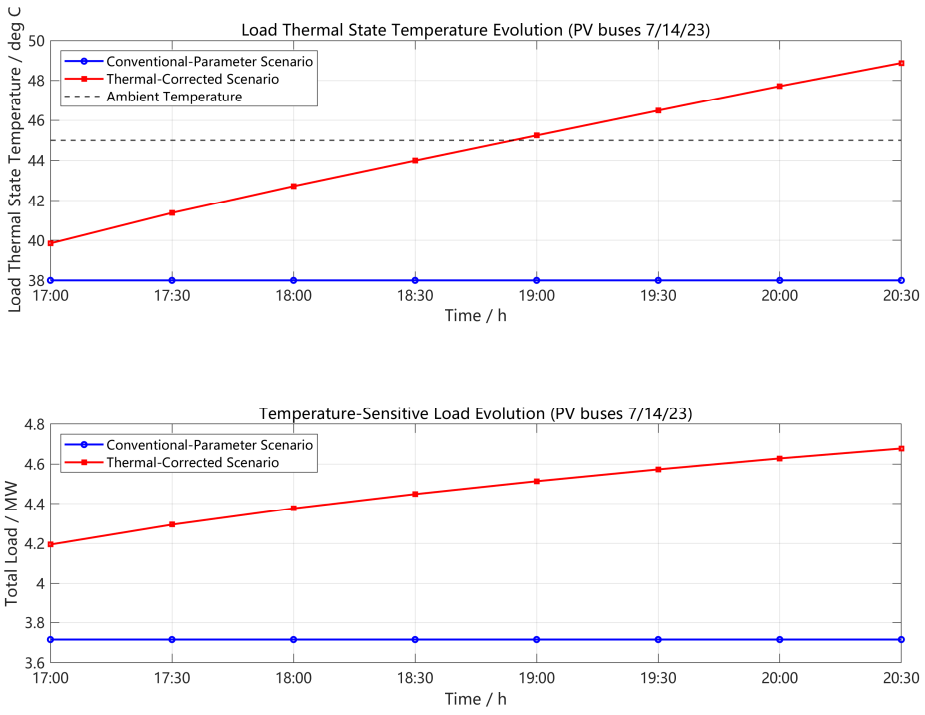


Figure 4. Evolution of temperature and temperature-sensitive load.

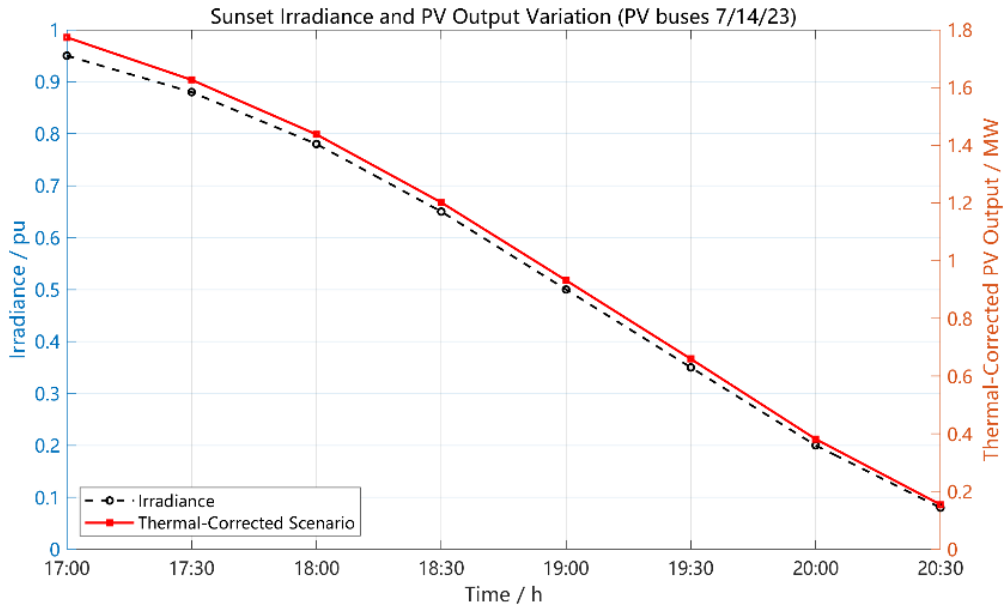


Figure 5. Solar power output variation and irradiance during sunset periods.

Figure 3 shows that under the thermally corrected scenario, the temperature of typical lines varies with time, and the line resistance increases compared to the conventional scenario. Under high-resistance operating conditions, the sensitivity of the terminal node voltage to load and PV output fluctuations is enhanced.

The results of temperature-sensitive load variation are shown in Figure 4. Under the conventional parameter scenario, the thermal state temperature of the load and the total load remain essentially stable, and after considering thermal accumulation, the thermal state temperature of the load continuously increases, and the total load rises accordingly. This phenomenon indicates that under extreme high temperature, the thermal storage effect of buildings delays the decline of air-conditioning loads, keeping load-side pressure at a relatively high level even after sunset. This characteristic exacerbates the supply pressure in the latter part of the evening peak period and drives the continuous accumulation of low-voltage risk.

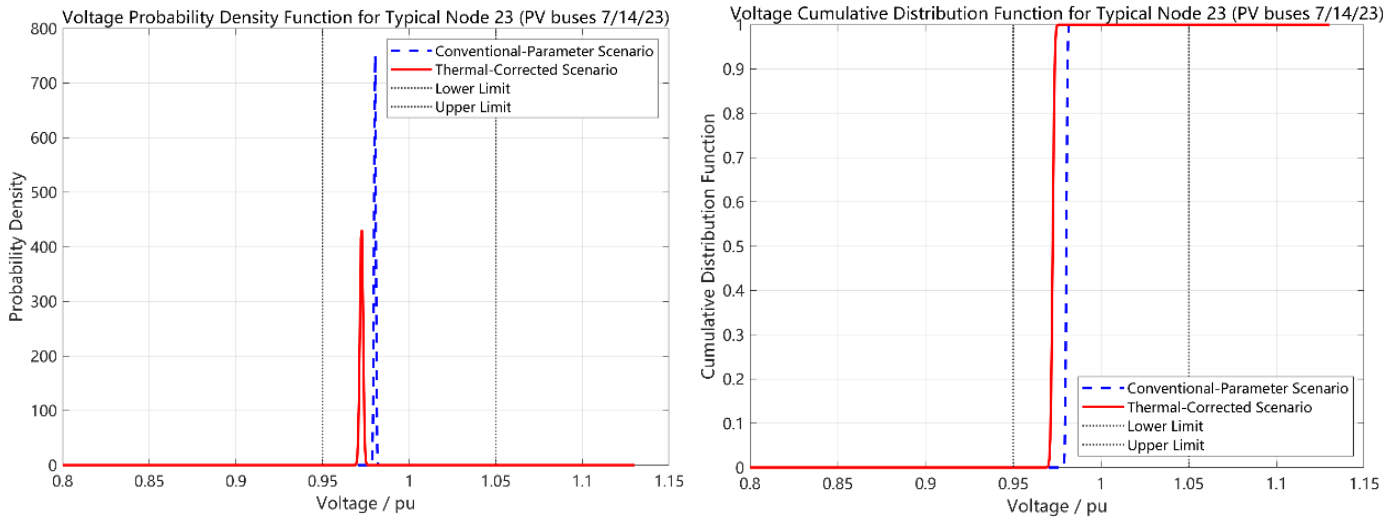
Figure 5 reflects the variation of PV output during the sunset period. As the irradiance decreases, the total distributed PV output continues to decline, and the local active power support capability gradually weakens. For PV sources connected to the middle and rear sections of the feeder, their output reduction directly weakens the terminal node voltage support; meanwhile, the module thermal derating caused by high temperature further reduces the available output, causing the supply-side support capability to decrease rapidly during the evening peak period.

5.2. Reconstruction of Node Voltage Probability Distribution and Analysis of Statistical Characteristics

To verify the applicability of the cumulant method combined with the Cornish–Fisher expansion for reconstructing nodal voltage probability distributions, Monte Carlo simulation is used as the reference benchmark. The Monte Carlo benchmark is generated using 10,000 independent random samples under the same source–load uncertainty model, electro-thermal correction parameters, and assessment snapshots as the proposed method. For an empirical cumulative probability estimated from $N = 10,000$ samples, the maximum standard error is $\sqrt{p(1-p)/N} \leq 0.005$, and the corresponding approximate 95% confidence half-width is less than 0.01. Therefore, the Monte Carlo CDF provides a sufficiently stable reference for assessing the accuracy of the Cornish–Fisher reconstruction. The cumulant Cornish–Fisher reconstruction uses the high-order voltage cumulants obtained from

the cumulant propagation procedure in Section 4. Specifically, cumulants up to the fifth order are retained in the numerical implementation to improve the approximation of tail behavior. The validation is first carried out at bus 23, which is a representative PV connection node, and is further extended to all network buses by comparing the voltage mean and standard deviation. The selected representative validation snapshot is 20:30, corresponding to the evening high-risk period when PV output decreases and temperature-sensitive load remains high due to thermal inertia.

Figure 6 shows under the conventional parameter scenario, the voltage distribution at bus 23 is relatively concentrated, with the probability density peak located in a higher voltage interval. After accounting for load thermal accumulation, line impedance temperature rise, and PV thermal derating, the voltage probability density curve under the thermally corrected scenario shifts as a whole toward the lower voltage direction, and the cumulative distribution curve shifts leftward accordingly. This result indicates that the high-temperature-related parameter corrections not only change the deterministic operating point of the node voltage but also alter the position of the voltage distribution under stochastic disturbances. Although the voltage at bus 23 has not yet exhibited an obvious limit violation, its voltage margin has already decreased to some extent, indicating that the thermal correction factors will weaken the local voltage support capability near the PV connection point.



(**a**) Voltage probability density function (PDF) (**b**) Voltage cumulative distribution function (CDF)

Figure 6. Comparison of voltage probability distribution at bus 23.

According to Figure 7, the results obtained by the Cornish–Fisher method and the Monte Carlo method are basically consistent. Quantitative calculations show that for typical bus 23, the maximum absolute error of the CDF is 4.10×10^{-3}, the root mean square error of the PDF is 0.5128, the absolute error of the voltage mean is 5.08×10^{-6} p.u., and the relative error of the standard deviation is 0.504%. From the statistical results of the entire network, the average absolute error of the voltage mean is 5.51×10^{-5} p.u., with a maximum error of 1.28×10^{-4} p.u., and the average absolute error of the voltage standard deviation is 1.27×10^{-5} p.u., with a maximum error of 3.59×10^{-5} p.u. The above errors are all small, indicating that this method can relatively accurately reconstruct the probability distribution and statistical characteristics of the node voltage. This comparison also supports the computational strategy adopted in this paper: the Cornish–Fisher reconstruction can achieve voltage distribution accuracy close to Monte Carlo simulation while

avoiding repeated nonlinear electro-thermal power-flow calculations for a large number of stochastic samples.

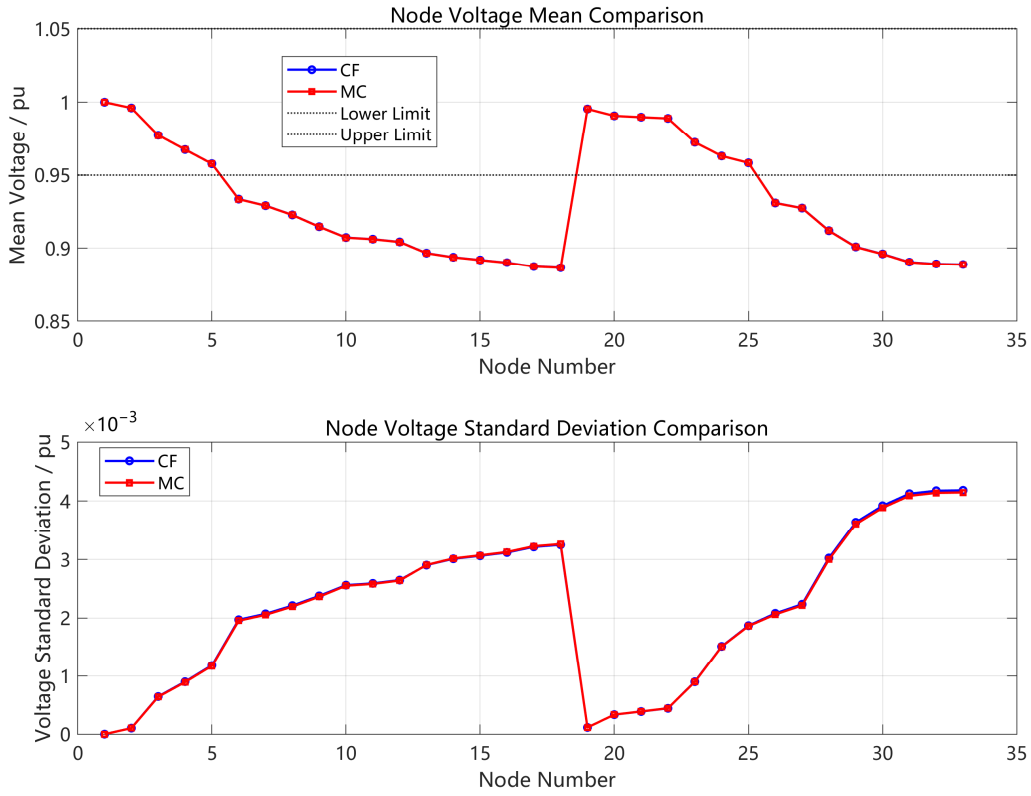


Figure 7. Comparison of nodal voltage statistical characteristics.

The Monte Carlo voltage samples in the studied high-temperature scenario exhibit continuous and single-peaked distributions, and no obvious multimodal or truncated voltage distribution is observed because no discrete voltage control switching or protection cut-off action is imposed in the probabilistic reconstruction. Therefore, the Cornish–Fisher expansion is applicable to the present assessment scenario. Nevertheless, its accuracy may decrease when the voltage distribution becomes strongly non-Gaussian, heavily tailed, multimodal, or truncated by discrete control and protection actions. In such cases, additional Monte Carlo verification or non-parametric density estimation should be employed.

5.3. Time-Series Evolution Analysis of System-Level Risk Factors

Figure 8 shows the temporal variation of the system average risk factor and the maximum node risk factor for the IEEE 33-bus system under the thermally corrected scenario. It can be observed that the system average risk factor began to rise significantly around sunset, rapidly climbed during the period from 17:30 to 20:30, and reached a peak of 0.330 at 20:30, which is higher than the 0.191 in the conventional parameter scenario, representing an increase of approximately 72%. The maximum node risk factor reached 0.410 over the same period, indicating that the low-voltage risk at terminal nodes was the most prominent. The peak low-voltage violation probability was 65.63%, and the peak scaled severity utility (×100) was 60.77, both of which are significantly higher than those in the conventional scenario.

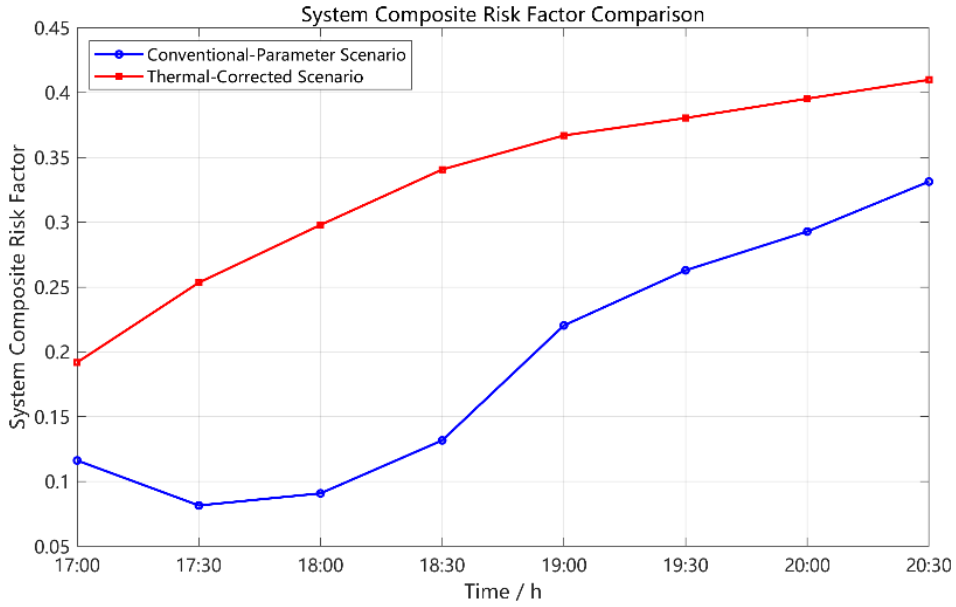


Figure 8. Temporal evolution of system-level risk factors under extreme heat.

The phase of rapid risk increase corresponds to the evening peak period when PV output drops rapidly while temperature-sensitive loads remain at a high level, indicating that the superposition of source–load mismatch and increased line impedance significantly compresses the voltage margin of terminal nodes. Overall, the system-level risk exhibits significant temporal dependence, and the latter part of the evening peak is the most prominent time window for system risk accumulation under high temperature.

Table 2 compares risk indicators for two scenarios. In the conventional scenario, the average engineering system composite risk factor is 0.191. The thermally corrected scenario increases this to 0.330. Peak low-voltage violation probability rises from 61.00% to 65.63%. The peak scaled severity utility ($\times 100$) increases from 33.44 to 60.77. The peak engineering system composite risk factor increases from 0.331 to 0.410. Both scenarios reach their peak at 20:30. The thermally corrected scenario shows higher risk across all measures.

Table 2. Comparison of system-level risk indicators under different scenarios.

Scenario	Average Engineering System Composite Risk Factor	Peak Low-Voltage Violation Probability (%)	Peak Scaled Severity Utility ($\times 100$)	Peak Engineering System Composite Risk Factor	Peak Time
Conventional parameter scenario	0.191	61.00	33.44	0.331	20:30
Thermally corrected scenario	0.330	65.63	60.77	0.410	20:30

To explicitly quantify the voltage violation error that would be overlooked without the proposed electro-thermal coupling model, the conventional parameter scenario is used as the non-coupled traditional power-flow benchmark, while the thermally corrected scenario represents the proposed electro-thermal coupled model. Two violation-count indicators are introduced. The deterministic number of violated buses is defined as $N_{vio}(t) = \sum_{i \in \Omega_L} 1\left(\overline{V}_i(t) < V_{\min}\right)$, where $\overline{V}_i(t)$ is the mean voltage of bus i. The expected number of violated buses is defined as $E[N_{vio}(t)] = \sum_{i \in \Omega_L} P_i^{low}(t)$. The cumulative violation counts over the assessment window are obtained by summing these indicators over all snapshots.

The comparison shows that the traditional non-coupled model underestimates both the spatial extent and the temporal accumulation of low-voltage violations. Without the proposed electro-thermal correction, the cumulative deterministic violation count is 90, whereas it increases to 150 after considering load thermal accumulation, transient conductor

thermal inertia, temperature-dependent line impedance, and PV thermal derating. Similarly, the cumulative expected violation count increases from 89.73 to 148.53. This means that 60 additional deterministic bus-time violation events and 58.80 additional expected bus-time violation events are identified by the proposed electro-thermal coupled model. Relative to the traditional non-coupled benchmark, the proposed model reveals a 65.5% increase in cumulative expected violation exposure. Equivalently, the traditional non-coupled model captures only about 60.4% of the cumulative expected violation exposure obtained by the electro-thermal coupled model. Therefore, the proposed methodology not only changes the calculated risk index but also reveals additional violation events that are overlooked by the traditional power-flow model.

5.4. Analysis of Dimensionless Severity Utility and Expected Violation Duration at Weak Nodes

Figures 9 and 10, respectively, show the scaled severity utility (×100) and the expected violation duration of typical weak nodes under the thermally corrected scenario. The dimensionless severity utility values of critical buses 18, 17, and 33 during the evening peak period reach 149.35, 145.96, and 140.50 after scaling by 100, respectively. These values should not be interpreted as physical voltage deviation percentages. Instead, they represent the nonlinear severity utility assigned by the exponential risk-preference function. Compared with the conventional parameter scenario, the thermally corrected scenario significantly increases the dimensionless severity utility of weak buses, indicating that deep low-voltage events are assigned much higher risk weights after the electro-thermal degradation of source, network, and load parameters is considered.

In terms of expected violation duration, the durations for buses 18 and 17 increased from approximately 133 min and 131 min in the conventional scenario to 236 min and 235 min, respectively, while both bus 33 and bus 32 lasted for 240 min, indicating that these buses remained in a low-voltage limit violation state for an extended period during the evening peak.

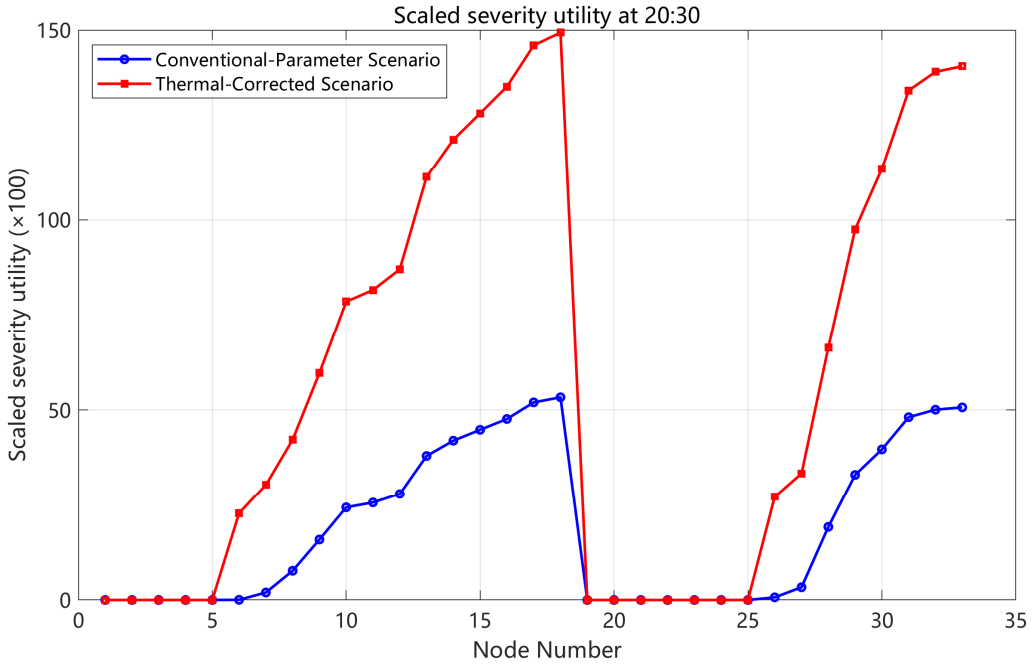


Figure 9. Scaled severity utility (×100) of critical weak buses during the evening peak.

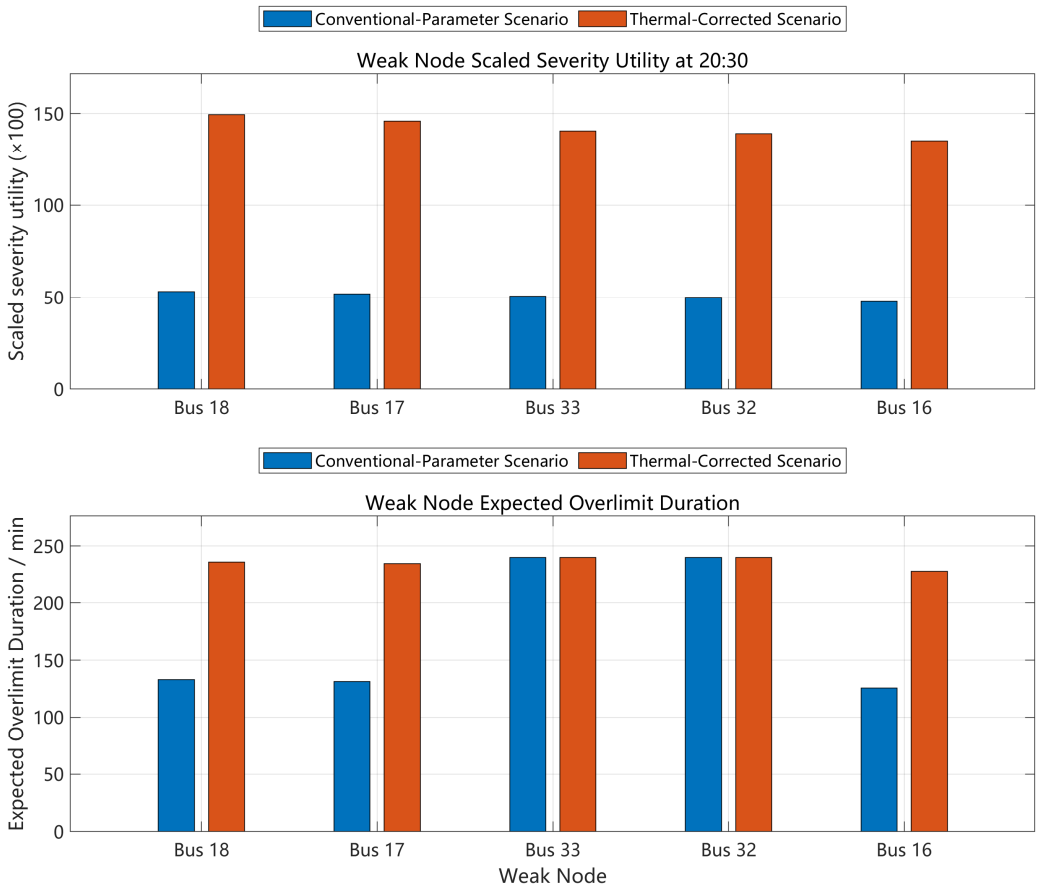


Figure 10. Scaled severity utility (×100) and expected violation duration of critical weak buses during the evening peak.

The quantitative evidence in Table 3 provides a direct basis for identifying the weakest buses and prioritizing mitigation actions during extreme heat events. As listed in Table 4, the five most critical weak buses are all located at the rear section of the main feeder or at the end of lateral branches, where the voltage drop accumulates most severely under the combined effect of thermal load growth and line resistance increase. In the thermally corrected scenario, the scaled severity utility (×100) of bus 18 reaches 149.35, while those of buses 17 and 33 are 145.96 and 140.50, respectively. These values are not physical voltage deviation percentages, but nonlinear severity utility values obtained from the exponential risk-preference function and scaled by 100 for presentation. In terms of temporal characteristics, the expected violation durations for buses 33 and 32 both reach 240 min, which is the maximum accumulated duration obtained from the eight 30 min assessment snapshots. This indicates that these two buses remain in a low-voltage risk state throughout the evaluated sunset and evening peak snapshots. Even bus 16 still has a scaled severity utility of 135.15 and an expected duration of 228.19 min. These results show that extreme high temperature not only elevates the probability of voltage violation but also increases the nonlinear severity utility and prolongs the expected violation duration.

The simultaneous increase in dimensionless severity utility and expected violation duration at terminal nodes indicates that under the thermally corrected scenario, the multiphysics coupling of source, network, and load has a significant impact on node vulnerability. Nodes in the rear section of the main feeder and at the ends of branches bear the most prominent voltage stress during the evening peak period, providing a quantitative basis for operation scheduling and risk warning under high-temperature conditions.

Table 3. Comparison of voltage violation counts between the traditional non-coupled power flow and the proposed electro-thermal coupled model.

Model	Peak Deterministic Number of Violated Buses	Cumulative Deterministic Violation Count	Peak Expected Number of Violated Buses	Cumulative Expected Violation Count	Peak Period
Traditional non-coupled power flow	20	90	19.52	89.73	20:30
Proposed electro-thermal coupled model	21	150	21.00	148.53	19:30–20:30

Table 4. Critical weak buses: scaled severity utility (×100) and expected violation duration.

Bus	Scaled Severity Utility Under Thermally Corrected Scenario (×100)	Expected Violation Duration Under Thermally Corrected Scenario/min
18	149.35	236.23
17	145.96	234.93
33	140.50	240.00
32	139.01	240.00
16	135.15	228.19

5.5. Sensitivity Analysis of the Risk-Preference Coefficient

To evaluate the influence of the risk-preference coefficient on the proposed voltage violation risk assessment results, a sensitivity analysis is conducted by varying γ around the baseline value of 0.582. The tested values are $\gamma = 0.30$, $\gamma = 0.582$, $\gamma = 0.80$, and $\gamma = 1.00$. Since the severity utility function used in this paper is $S(\omega_i) = \gamma(e^{\omega_i} - 1)$, changing γ scales the dimensionless severity utility and the comprehensive risk factor proportionally, while the monotonicity and convexity of the utility function remain unchanged.

Table 5 shows the relative system-level risk and weak node ranking under different values of γ. The baseline case $\gamma = 0.582$ is used as the reference. As γ increases, the system-level comprehensive risk factor increases proportionally, indicating that a more risk-averse preference assigns larger weights to low-voltage consequences. However, the ranking of critical weak buses remains unchanged, and the top five weak buses are consistently identified as buses 18, 17, 33, 32, and 16. This indicates that the proposed weak node identification result is not sensitive to the specific scaling coefficient, although the absolute magnitude of the comprehensive risk factor changes with the selected risk preference.

Table 5. Sensitivity analysis of the risk-preference coefficient γ.

γ	Relative System Average Risk $R_{sys}(\gamma)/R_{sys}(0.582)$	Maximum-Risk Bus	Top 5 Weak Buses	Ranking Stability
0.30	0.516	Bus 18	18, 17, 33, 32, 16	Unchanged
0.582	1.000	Bus 18	18, 17, 33, 32, 16	Baseline
0.80	1.375	Bus 18	18, 17, 33, 32, 16	Unchanged
1.00	1.718	Bus 18	18, 17, 33, 32, 16	Unchanged

The sensitivity results demonstrate that γ mainly affects the numerical scale of the comprehensive risk factor, rather than the spatial identification of vulnerable buses. Therefore, the main conclusion that the thermally corrected scenario significantly increases the voltage violation risk of feeder-end weak buses remains robust under different risk-preference settings.

5.6. Computational Efficiency and Scalability Discussion

The scalability of the proposed electro-thermal probabilistic risk assessment method is mainly affected by two parts: the deterministic electro-thermal power-flow iteration and the stochastic uncertainty propagation. In a sample-based Monte Carlo or LHS framework, the conductor temperature, temperature-dependent resistance, network admittance matrix, and Jacobian matrix need to be updated repeatedly for each stochastic sample. This leads to a high computational burden when the number of samples and the network size increase.

In contrast, the proposed method performs the electro-thermal iteration only at the deterministic reference operating point of each assessment snapshot. After the conductor temperature and line resistance converge, the admittance matrix and voltage sensitivity matrix are updated once. The stochastic propagation of load and PV uncertainties is then completed analytically by the cumulant method and Cornish–Fisher expansion. Therefore, the computational burden is mainly related to the number of assessment snapshots and electro-thermal iterations, rather than the number of stochastic samples.

The computational mechanism of the proposed method is compared with that of sample-based electro-thermal probabilistic power flow in Table 6.

Table 6. Comparison of computational mechanisms between sample-based electro-thermal probabilistic power flow and the proposed method.

Method	Electro-Thermal Iteration	Matrix Update	Uncertainty Propagation	Main Computational Burden
Monte Carlo/LHS electro-thermal probabilistic power flow	Performed for each random sample	Updated for each sample and each thermal iteration	Statistical estimation from samples	$N_t N_s K_{th} C_{PF}(N)$.
Proposed cumulant-Cornish–Fisher method	Performed only at each assessment snapshot	Updated after convergence of the reference electro-thermal state	Analytical propagation using cumulants	$N_t K_{th} C_{PF}(N) + N_t C_{cum}(N)$.

The comparison in Table 6 indicates that the main computational advantage of the proposed method comes from separating the reference electro-thermal correction from the stochastic uncertainty propagation. In the Monte Carlo or LHS framework, each random sample may require repeated updates of conductor temperature, line resistance, admittance matrix, and Jacobian matrix. In the proposed method, these updates are carried out only at the thermally corrected reference operating point of each assessment snapshot. The subsequent uncertainty propagation is completed through voltage cumulants and the Cornish–Fisher reconstruction. Therefore, the number of repeated nonlinear electro-thermal power-flow calculations is greatly reduced.

The present numerical validation is performed on the IEEE 33-bus distribution system. This feeder is suitable for verifying the physical mechanism, the proposed risk indices, and the accuracy of the cumulant Cornish–Fisher reconstruction under an extreme high-temperature scenario. However, this test does not fully represent the computational conditions of large practical distribution networks. Further validation on larger feeders, such as the IEEE 123-bus system and the 8500-node distribution test feeder, is still needed to evaluate the real-time applicability of the proposed framework.

6. Conclusions

This paper targeted the voltage limit violation risk in distribution networks under extreme high temperature and established a source–network–load multiphysics coupling model and a comprehensive risk assessment method. Based on the simulation of an extreme high-temperature scenario on the IEEE 33-bus system, the following conclusions are drawn.

The proposed method, by integrating the violation probability and severity, can continuously characterize the risk variation during the node voltage drop process, and can reflect the system risk level more comprehensively compared to binary limit violation judgments.

Under extreme high temperature, the decline in PV output, the high level of temperature-sensitive loads, and the deterioration of line parameters jointly caused the low-voltage limit violation risk to continuously rise in the latter part of the evening peak. The high-risk areas were concentrated at the rear section of the main feeder and at the ends of branches. Terminal weak nodes should be the focus of risk warning and operational defense during high-temperature weather.

Although the proposed method reduces the computational burden by avoiding repeated electro-thermal power-flow calculations for individual stochastic samples, the numerical validation in this paper is still limited to the IEEE 33-bus distribution system. Large-scale verification on practical feeders, such as the IEEE 123-bus system and the 8500-node distribution test feeder, will be carried out in future work to further evaluate the scalability and real-time applicability of the proposed multiphysics risk assessment framework.

In addition, the present study adopted a constant power approximation for aggregated temperature-sensitive loads to represent a conservative low-voltage risk condition. In practical distribution networks, some air-conditioning and electronically controlled loads may exhibit voltage-dependent ZIP characteristics or protection-related disconnection behavior. Future work will incorporate ZIP load models and protection-constrained load response models to further evaluate the robustness of the proposed voltage violation risk assessment framework.

Author Contributions: Conceptualization, J.H. and Q.C.; methodology, Q.C.; software, Q.C.; validation, Q.C. and P.Y.; formal analysis, Y.L.; investigation, X.N.; data curation, S.W. and H.D.; writing—original draft preparation, Q.C.; writing—review and editing, Q.C.; visualization, Q.C. All authors have read and agreed to the published version of the manuscript.

Funding: This research received no external funding.

Data Availability Statement: All data generated or analyzed during this study are included in this published article.

Conflicts of Interest: The authors declare no conflicts of interest.

Nomenclature

$P_i(t)$	Active power of temperature-sensitive load at node i
P_i^{base}	Baseline load at node i
α_i	Load temperature sensitivity coefficient of node i
$\Delta T_{eff}(t)$	Effective indoor–outdoor temperature difference
$R(T)$	Conductor resistance at temperature T
R_0	Resistance at baseline temperature T_0
α_R	Temperature coefficient of resistance
T_c	Actual conductor operating temperature
ΔV	Branch voltage magnitude loss
P, Q	Branch active/reactive power flow
Z	Branch impedance
V_N	Rated voltage
P_{PV}	PV output power after thermal derating
η_{ref}	Rated conversion efficiency
A	Equivalent module area
$G(t)$	Real-time irradiance
γ	Power temperature derating coefficient
T_{STC}	Standard test temperature
T_{cell}	PV cell temperature
I_i	Injected current phasor at constant power load node
V_i	Node voltage phasor
P_i^{load}, Q_i^{load}	Active/reactive power demand of constant power load
P_i, Q_i	Active/reactive power injection at node i
$\overline{P}, \overline{Q}$	Expected values of baseline injected power after thermal correction
$\Delta P_i^{err}, \Delta Q_i^{err}$	Multiplicative random factors of injected power
$\psi_X(t)$	Cumulant generating function

$E[\cdot]$	Mathematical expectation operator
V_0	Deterministic reference operating point voltage vector
ΔV	Node voltage micro-increment vector
ΔS	Injected power micro-increment vector
J	Voltage-to-power sensitivity matrix
$\gamma_{\Delta V}^{(k)}$	k-th-order semi-invariant vector of node voltage magnitudes
$\gamma_{\Delta S}^{(k)}$	k-th-order semi-invariant vector of injected power
ξ_i	Standardized voltage variable of node i
μV_i	Expected value of node voltage
σV_i	Standard deviation of node voltage
$z(\alpha)$	Quantile of standard normal distribution
γ_3, γ_4	Skewness and kurtosis coefficients
$f_i(v)$	Probability density function (PDF) of voltage at node i
$F_i(v)$	Cumulative distribution function (CDF) of voltage at node i
D_{sys}	System average physical voltage violation depth
$T_{sys}^{\exp}$	System average expected violation duration
R_{sys}	System average risk factor
$R_{\max}$	Maximum node risk factor
m_l	Conductor mass per unit length of branch l
$c_{p,l}$	Specific heat capacity of conductor l
$q_{s,l}$	Solar heat gain of conductor l
$q_{c,l}$	Convective heat loss of conductor l
$q_{r,l}$	Radiative heat loss of conductor l
K_{th}	Average number of electro-thermal iterations
$C_{PF}(N)$	Computational cost of one deterministic power-flow solution for an N-node network
$C_{cum}(N)$	Computational cost of cumulant propagation and Cornish–Fisher reconstruction
$N_{vio}(t)$	Deterministic number of violated buses at time t
$E[N_{vio}(t)]$	Expected number of violated buses at time t
γ	Risk-preference scaling coefficient
$\eta_i(t)$	Physical low-voltage violation depth of node i
$\overline{\eta}_i(t)$	Conditional average physical voltage violation depth
$T_i^{\exp}$	Expected violation duration of node i
N_{MC}	Number of Monte Carlo samples
c_L	Coefficient of variation of load random multiplier
c_{PV}	Coefficient of variation of PV random multiplier/normalized PV output ratio
T_{set}	Indoor temperature setpoint
$C_{b,k}$	Equivalent building thermal capacitance
$R_{b,k}$	Equivalent building thermal resistance
$Z_{PV,i,t}$	Normalized PV output ratio at node i and snapshot t
$\mu_{PV,i,t}$	Normalized mean of PV output ratio
$\sigma_{PV,i,t}^2$	Variance of normalized PV output ratio
$\alpha_{PV,i,t}, \beta_{PV,i,t}$	Shape parameters of the Beta distribution
$\xi_{PV,i,t}$	Mean-1 PV multiplicative random factor
D_l	Equivalent conductor diameter of branch l
α_s	Solar absorptivity of conductor surface
σ_{SB}	Stefan–Boltzmann constant

Abbreviations

The following abbreviations are used in this manuscript:

PV	Distributed Photovoltaic
PDF	Probability Density Function
CDF	Cumulative Distribution Function
IEEE	Institute of Electrical and Electronics Engineers
DG	Distributed Generation
DER	Distributed Energy Resource

CDF(error)	Maximum Absolute Error of Cumulative Distribution Function
RMSE	Root Mean Square Error

References

1. Wang, Y.; Wang, H.; Cui, P.; Chen, D.L.; Tang, J.B.; Ou, Y.H.; Hao, J.S.; Wang, J.; Zhang, G.T.; Lei, Y.; et al. Disaster effects of climate change and the associated scientific challenges. *Chin. Sci. Bull.* **2024**, *69*, 286–300. (In Chinese) [CrossRef]
2. Zhou, Y.R.; Mao, Y.X.; Hu, Y.; Tian, R.; Huang, W.B.; Ma, G.W. Impacts of extreme weather on Sichuan power in summer of 2022 and its enlightenment. *J. Hydroelectr. Eng.* **2023**, *42*, 23–29. [CrossRef]
3. Liang, Z.F.; Kang, C.Q.; Sui, L.F.; Yu, R.Y.; Jia, Y.X.; Du, Y.L.; Chen, W.J. Research on risk warning and prevention strategies for main distribution networks with high proportion distributed photovoltaics. *J. Tsinghua Univ. (Sci. Technol.)* **2024**, *64*, 1964–1978. [CrossRef]
4. Luo, J.Y.; Xing, H.J.; Quan, W.B.; Shi, Y.Q. Resilience assessment and differentiated planning of new power systems under extreme high temperatures. *Autom. Electr. Power Syst.* **2025**, *49*, 135–144. [CrossRef]
5. Zheng, H.F.; Liu, Q.; Yao, L.; Zhang, Y.; Zou, Y.C.; Hu, Z.D.; Wang, Y.; Dai, T.L. Probabilistic assessment of supply-demand balance capability in new power systems for extreme high temperature scenarios. *Electr. Power* **2026**, *59*, 44–56. [CrossRef]
6. Tian, S.X.; Xiao, W.Y.; Fu, Y.; Zhou, J.; Li, Z.K.; Mi, Y. Boosting Resilience of Cable Distribution Networks Under Extreme High-temperature Disaster. *Proc. CSEE* **2025**, *45*, 3408–3420. [CrossRef]
7. Zhou, X.M.; Ge, S.Y.; Li, T.; Liu, H. Assessing and boosting resilience of distribution system under extreme weather. *Proc. CSEE* **2018**, *38*, 505–513+681. [CrossRef]
8. Ji, G.L.; Yuan, Y.; Fan, X.R.; Yuan, R.M.; Ling, K.Y.; Li, X. Risk assessment of voltage limit violation on distribution network based on Cornish-Fisher expansion. *Acta Energiae Solaris Sin.* **2020**, *41*, 358–366. [CrossRef]
9. Huang, Y.; Li, Z.X.; Hu, S.L.; Teng, T.Y.; Wang, Y.; Tan, C. Risk assessment of distribution network based on sparse polynomial chaos expansion with Lasso regression. *Chin. J. Eng.* **2026**, *48*, 1300–1311. [CrossRef]
10. Ma, H.Y.; Li, G.; Wang, H.; Yan, Z.; Xu, X.Y. Probabilistic evaluation of photovoltaic hosting capacity in unbalanced distribution network via polynomial chaos based Kriging model. *IEEE Trans. Ind. Appl.* **2025**, *61*, 1466–1474. [CrossRef]
11. Guimaraes, I.O.; Silva, A.M.L.d.; Nascimento, L.C.; Fotuhi-Firuzabad, M. Reliability assessment of distribution grids with DG via quasi-sequential Monte Carlo simulation. *Electr. Power Syst. Res.* **2024**, *229*, 110156. [CrossRef]
12. Wanjoli, P.; Moustafa, M.M.Z.; Abbasy, N.H. Probabilistic power flow analysis of DERs integrated power system from a Bayesian parameter estimation perspective. *IEEE Access* **2024**, *12*, 178734–178750. [CrossRef]
13. Huang, W.; Hu, B.; Shao, C.Z.; Li, W.; Wang, X.Z.; Xie, K.G. Power system reliability evaluation based on sequential Monte Carlo simulation considering multiple failure modes of components. *J. Mod. Power Syst. Clean Energy* **2025**, *13*, 202–214. [CrossRef]
14. Ayaz, M.S.; Malekpour, M.; Azizipanah-Abarghooee, R.; Karimi, M.; Terzija, V. Probabilistic photovoltaic generation and load demand uncertainties modelling for active distribution networks hosting capacity calculations. *Int. J. Electr. Power Energy Syst.* **2024**, *159*, 110081. [CrossRef]
15. Ghazanfariharandi, M.; Mieth, R. Analysis of data value in stochastic optimal power flow for distribution systems. *IEEE Trans. Smart Grid* **2025**, *16*, 3377–3391. [CrossRef]
16. Liu, H.P.; Yang, X.J.; Lu, T.; Ma, G.; Lu, X.D.; Li, Z.B.; Zheng, X.L. A method for constructing a risk assessment indicator system for grid operation considering distributed new energy source. *Zhejiang Electr. Power* **2024**, *43*, 1–14. [CrossRef]
17. Guan, Q.Y.; Zheng, X.; Xu, J.Y.; Xiong, Y.; Guo, T.; Li, J.Y.; Zhang, W.C.; Liu, Z.Y. An operation optimization model of receiving power grid considering security risk assessment under large-scale new energy access. *Renew. Energy Resour.* **2023**, *41*, 957–963. [CrossRef]
18. Zhang, J.Q.; Yu, S.S.; Xu, L.H. Research on the control method of distributed photovoltaic power generation output in novel power system considering the voltage over-limit risk. *Electr. Meas. Instrum.* **2026**, *63*, 11–23. [CrossRef]
19. Zhang, Y.J.; Lin, L.X.; You, Z.W.; Liang, X.Y. Distributed model free voltage control for distribution networks with high percentage of distributed PV systems. *Acta Energiae Solaris Sin.* **2025**, *46*, 209–219. [CrossRef]
20. Ou, Y.H.; Jiang, T.; Zhang, Y.H.; Liang, C.; Ma, X.P.; Liu, W.Y. Multi-time scale voltage control method of distribution network with high-penetration distributed PV considering reactive power regulation of converter. *Electr. Power Autom. Equip.* **2024**, *44*, 221–230. [CrossRef]
21. Sun, W.H.; Pan, M.; Zhu, N.; Lu, W.H.; Xu, M.X.; Jiang, F.X. Analysis and countermeasures of overvoltage problems in distribution networks under high-proportion distributed photovoltaic access conditions. *Transformer* **2025**, *62*, 47–54. [CrossRef]
22. Chen, P.W.; Xiao, X.N.; Baran, M. Complex affine arithmetic based power flow algorithm for weak-mesh distribution network considering reactive power characteristics of distributed generator. *Autom. Electr. Power Syst.* **2019**, *43*, 59–66. [CrossRef]
23. Wang, B.Y.; Pi, J.B.; Wang, X.L.; Qi, S.X.; Sun, W.D.; Huang, Q.H.; Wei, C.X.; Zhang, X.P.; Xu, X.R.; Wang, Z.X. A fast assessment method for supply-demand imbalance risk of new power systems based on deep active learning driven by weather data. *Power Syst. Technol.* **2024**, *48*, 4050–4060. [CrossRef]

24. Xu, C.Y.; Yang, J.; Dou, Z.L.; Zhang, Y.W.; Zhu, X. Research on distribution network and microgrid-level integrated energy system intraday rolling scheduling technology based on data-driven robust optimization. *Eng. J. Wuhan Univ.* **2025**, *58*, 1206–1216. [CrossRef]
25. Li, L.; Song, H.H.; Yan, Z.B.; Li, H.Y.; Jin, P.L.; Zhao, J.Q. A two-stage robust optimization strategy for microgrids considering the grid-forming capability of energy storage and uncertainties of wind, photovoltaic, and load. *J. Energy Storage* **2025**, *140*, 115678. [CrossRef]
26. Yang, X.; Shang, J.Y.; Zhang, Z.P.; Wang, G.; Zhao, J.P.; Ding, B.P. Robust optimization dispatch for PV rich power systems considering demand response and energy storage systems. *Front. Energy Res.* **2024**, *12*, 1456789. [CrossRef]
27. Chai, Y.Y.; Zhao, X.B.; Lv, C.X.; Liang, T.L.; Dong, Y.C. Coordinated multi-time scale optimal regulation for source-grid-load-storage of distribution network based on Fisher period division. *Power Syst. Technol.* **2024**, *48*, 1593–1606. [CrossRef]
28. Zhao, P.J.; Wu, J.Y.; Zhang, W.H.; He, S.; Zhang, H.S. Cooperative peer to peer scheduling of multi-microgrids considering distribution network power flow and source-load uncertainty. *Power Syst. Technol.* **2022**, *46*, 4885–4896. [CrossRef]
29. Zhao, R.F.; Wu, R.H.; Lu, J.G.; Chen, F.C.; Li, Q.W. Scenario-based optimized coordinated scheduling of transmission and distribution networks with multiple timescales considering renewables correlations. *IEEE Access* **2025**, *13*, 115367–115383. [CrossRef]
30. Zhang, X.; Ying, Z.; Chen, Y.; Chen, X. A Thermal Model for Calculating Axial Temperature Distribution of Overhead Conductor under Laboratory Conditions. *Electr. Power Syst. Res.* **2019**, *166*, 223–231. [CrossRef]
31. Riba, J.-R. Radial Thermoelectric Model for Stranded Transmission Line Conductors. *Sensors* **2023**, *23*, 9205. [CrossRef] [PubMed]

Disclaimer/Publisher's Note: The statements, opinions and data contained in all publications are solely those of the individual author(s) and contributor(s) and not of MDPI and/or the editor(s). MDPI and/or the editor(s) disclaim responsibility for any injury to people or property resulting from any ideas, methods, instructions or products referred to in the content.